ORIGINAL RESEARCH ARTICLE

Changes in Microscale Liquid Formation in Lump and Sinter Mixed Burden Softening and Melting Tests with the Addition of Hydrogen

NATHAN BARRETT, SUBHASISH MITRA, EVAN COPLAND, SHENG CHEW, DAMIEN O'DEA, and TOM HONEYANDS

With the movement toward hydrogen-enriched blast furnace operation to lower greenhouse gas emissions, ferrous burden design must be reconsidered to optimize furnace permeability. Increasing the ratio of direct charge lump ore in the ferrous burden also presents an opportunity to lessen the emissions associated with the production of sinter and pellets. Under traditional blast furnace conditions, lump ore usage is improved by mixing it with the sinter in the burden to promote their favorable high-temperature interactions (both chemical and physical). As such, mechanistic changes to the interaction must be understood to optimize burden design, including for future operations with hydrogen addition. In this study, liquid formation in both the metallic and oxide components of ferrous burdens is microscopically investigated. Oxide liquid and solid phase stability at the interfaces of dissimilar burdens are visualized using a novel mapping technique, and metallic iron is etched to reveal microstructures indicative of carbon. Results indicate that the inclusion of hydrogen promotes the gas carburization of metallic iron in sinter, but not lump. It was concluded that mixed burden softening and melting performance with hydrogen addition were improved through the addition of lump in two ways: the highly metallic lump particles provide structural support for the collapsing sinter bed and also suppress the formation of early liquid slag from the sinter.

NATHAN BARRETT, SUBHASISH MITRA, EVAN COPLAND, and TOM HONEYANDS are with the Centre for Ironmaking Materials Research, School of Engineering, The University of Newcastle, Callaghan, NSW 2308, Australia and also with the 70 Vale St, Shortland, NSW 2307, Australia. Contact e-mail: tom.a.honeyands@newcastle.edu.au SHENG CHEW is with the BlueScope, Coke & Ironmaking Technology, Port Kembla, NSW 2505, Australia and also with the PO Box 1854, Wollongong, NSW 2500, Australia. DAMIEN O'DEA is with BHP, 480 Queen St, Brisbane, QLD 4000, Australia.

Manuscript submitted November 12, 2023; accepted February 25, 2024.

Published online: 28 March 2024

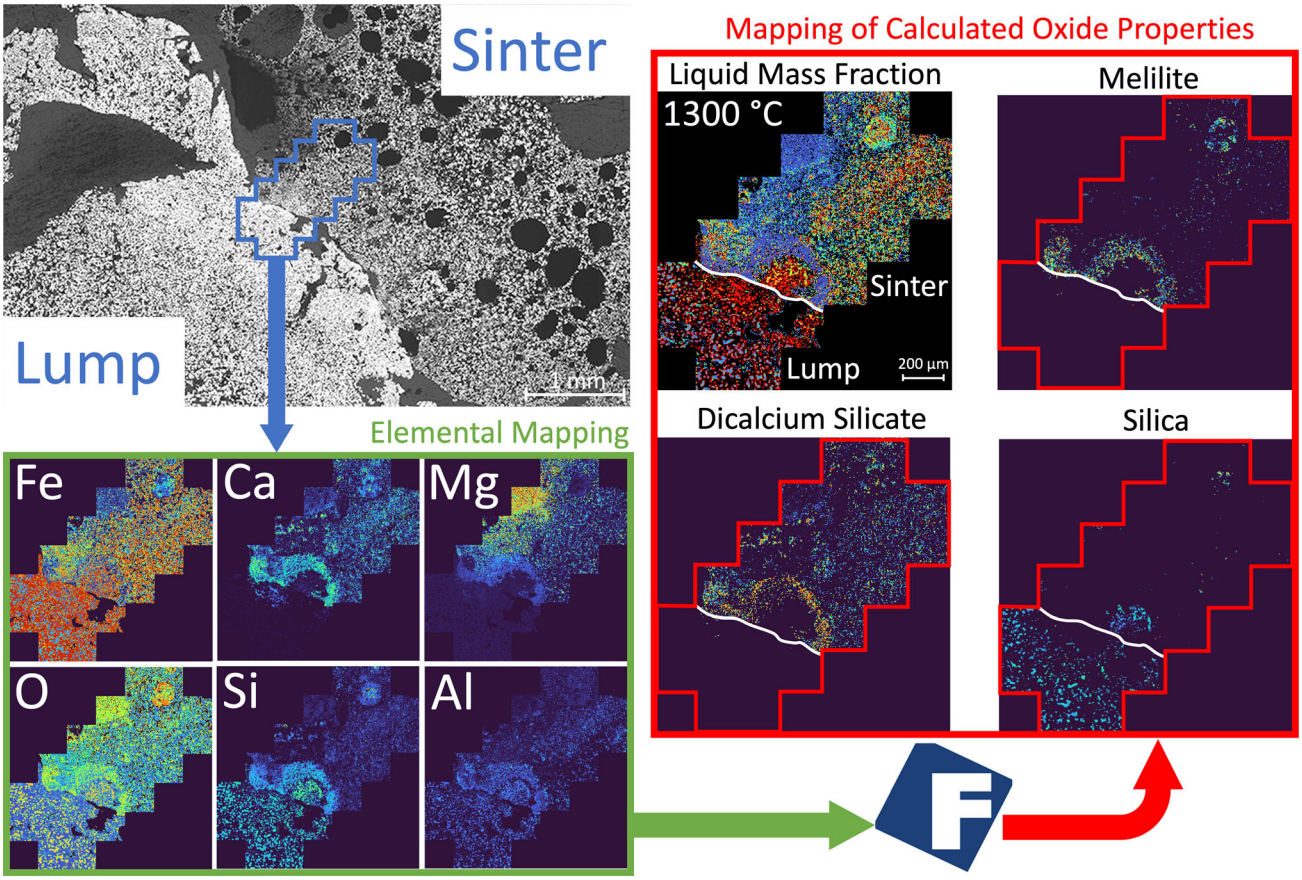

https://doi.org/10.1007/s11663-024-03062-w

I. INTRODUCTION

IRONMAKING blast furnace technology has evolved over hundreds of years, with enormous improvements in energy efficiency and operation scale since its conception.[1] Global pressures to reduce greenhouse gas emissions make hydrogen-enrichment a natural next step in the blast furnace evolution. Enrichment of the blast furnace with hydrogen stands to change its internal conditions. Of key importance is the formation characteristics of the cohesive zone in which ferrous burden softens and melts, restricting gas flow and hindering productivity. As such, rigorous understanding of ferrous burden behavior under hydrogen-enriched conditions is required.

While sinter and pellet are traditionally used for their desirable high-temperature characteristics, increasing the proportion of direct charge lump ore can decrease the emissions associated with sinter and pellet production. In modern operations, use of up to ~ 20 pct lump ore[2] and higher is facilitated by its favorable high-temperature interactions (both chemical and physical) when mixed with sinter.[3] As such, a mechanistic understanding of the impact of hydrogen on the interaction between lump and sinter will be required to optimize burden design in future operations.

At a high level, the mechanism of interaction between slag phases under traditional conditions is understood. The chemical interaction between lump and sinter is driven by a difference in composition: the primary gangue components in lump ore are silica (SiO_2) and alumina (Al_2O_3), while sinter contains added flux–lime (CaO) and magnesia (MgO). The primary slag composition of lump ore is strongly dependent on the degree of reduction, which dictates the amount of wustite (FeO) remaining to participate in slag formation. Under typical conditions, sufficient FeO remains in the lump at the onset of melting to form low-temperature fayalitic (FeO/SiO_2 based) melts,[3–5] with the remaining gangue associating with high-temperature phases such as mullite ($Al_4SiO_8/Al_6Si_2O_{13}$)[4] and spinel ($FeAl_2O_4$).[3] In mixed burdens, slag components (particularly calcium) have been observed to migrate across the boundaries of lump and sinter particles,[3,6–10] initiated by low-temperature

liquid formation (~ 1200 °C).[3,9] The interaction between liquid slag and gangue at the interfaces of dissimilar burdens raises the solidus temperature of the generated liquids,[10] re-solidifying them[9] and forming new gangue phases such as olivine ($CaFeSiO_4$).[3,7] Further increase in temperature (> 1300 °C) promotes liquid formation in the new phases, allowing additional migration of elements and resulting in final slag phases such as merwinite ($Ca_3MgSi_2O_8$) and melilite (mainly akermanite ($Ca_2MgSi_2O_7$) and gehlenite ($Ca_2Al_2SiO_7$)).[7] Increasing the content of hydrogen in the blast furnace will likely alter the ferrous burden degree of reduction at the onset of melting. This will impact both the composition of the primary slag (and thus first liquid generation temperature) and secondary slags generated during interaction. Some studies have observed that the interaction between burdens still occurs at higher degrees of reduction, however, the onset temperature increased and intensity weakened.[11] Changes in the mechanisms of interaction at high degrees of reduction remain largely unexplored.

During its descent in the furnace stack, ferrous burden is reduced past the composition of wustite (FeO) resulting in metallic iron growth within the particles, the morphology of which is dependent on both the texture inherited from the original ore used and the porosity acquired during and reduction.[12,13] At the microscale, the growth of crystalline metallic iron in the particles forces oxide gangue to segregate into a separate phase.[13] As such, the ferrous burden microstructure as it begins melting is one of the partitioned networks of metallic iron interspersed with oxide gangue (slag) and pores.[13–15] The liquid formation characteristics of both the slag and iron phases contribute to the softening and melting performance of the ferrous burden in the cohesive zone.[16]

The melting properties of the slag phases are primarily related to their composition, which can vary between burden types and within individual particles. With the partitioning of metallic and oxide systems within the particle at the microscale, first liquid formation becomes a microscopically local occurrence.

The melting properties of the metallic iron phase are dominated by its carbon content, which can dissolve in the metallic phase through multiple mechanisms.[17–20] Analysis of liquid formation in the metal phase under traditional conditions is typically secondary to slag, as unless carbon is present in the metallic iron phase its melting point will likely be much higher than those of the first liquid slags. However, the addition of hydrogen has been suggested to impact the gas carburization of iron during its reduction, and thus its melting point.[21,22] As such, to comprehensively understand the contribution of metal meltdown to softening and melting performance, the carbon content of the metal must be determined. One method for doing so is metallographic etching,[23,24] which is advantageous as it preserves the spatial distribution of carbon in the sample.

Samples of lump and sinter are heterogenous in nature so local conditions in the packed bed will determine what interactions occur. Analysis based on bulk assay and overall degree of reduction, while useful as an approximation, may miss important details. Use of SEM techniques to obtain a small number of point analyses is an improvement but may still miss some of the rich details present in the system. This work aims to analyze every point in a region of interest, calculate equilibrium phase proportions and composition, and map the determined properties back onto the micrograph allowing the mechanisms of interaction to be investigated.

Various techniques have been employed historically to elucidate the mechanisms of slag phase interaction.[3,4,6–11,25–29] However, elemental mapping techniques (such as SEM-EDS[6,9,10,27–30] and EPMA[3,8]) have only been used separately to thermodynamic calculations. Estimation of liquid formation with thermodynamic packages (such as FactSage)[4,5,7–9,25,27] or ternary/pseudo-ternary phase diagrams[4–6,11,29] is typically done using bulk chemical analysis (of initial material[8,9,27] or collected slags[4,5,7,25]) or point analysis.[4,29] Calculations using bulk chemistry may be particularly susceptible to the calculated overall degree of reduction, which may not apply to local interfaces, where the interaction actually occurs. With the heterogenous distribution of elements (including FeO) both within and between particles, thermodynamic analysis in this manner is restricted in its spatial application to the microscale system in which liquid is first formed and propagated.

In a previous study, the authors reported observations on the effect of hydrogen addition on the softening and melting test performance of lump, sinter, and lump/sinter mixed burdens.[22] It was demonstrated that with hydrogen addition, the lump ore pressure drop improved, while the sinter pressure drop deteriorated. Of importance, mixed burdens indicated that a favorable high-temperature interaction still occurred between burdens with the inclusion of hydrogen.

This study aims to provide detailed analysis of both the slag and metallic iron phases to further explain the previously reported experimental observations. For the oxide slag system, the primary investigation is into local interfacial conditions and their liquid formation and interaction characteristics. For the metallic iron system, the primary investigation is into the change in carbon content. For all analysis, particular attention is given to preserving the spatial distribution of elements at temperatures before the onset of full meltdown.

II. METHODOLOGY

A. *Softening and Melting Test*

Samples from previously reported softening and melting tests were used for analysis in this study. To summarize: two burden types were used (the same as in a previous line of work[22]), namely a high basicity plant sinter (SH1) and Newman Blend Lump (NBLL, a

high-grade hematite–goethite Australian lump ore). Burdens comprised of NBLL, SH1, and 20 pct NBLL and 80 pct SH1 (mixed burden, MB1) were tested under reducing gas compositions of 30 pct CO, 70 pct N_2 (Base Case gas) and 30 pct CO, 15 pct H_2, 55 pct N_2 (Hydrogen Case gas). The bulk chemical composition of the burdens is shown in Table I. Some tests were interrupted at select temperatures and the crucibles set in resin. The crucibles were then sectioned longitudinally to attain insight into the physical structure at temperature through reflected light microscopy.

This study further analyses select interrupted samples to provide insight into the chemical and metallurgical structures present at temperature. Specifically, softening and melting test samples that were interrupted at a sample temperature of 1300 °C were chosen for detailed analysis. This temperature was chosen as it preceded the sharp spike in pressure drop and full meltdown of the burden. As such, formation of interfaces in mixed burdens at which only primary slags had interacted could be assessed before large dynamic movement/mixing of liquid (melting of secondary slag). Additionally, the presence of carbon in the metal could be determined prior to the formation of liquid metal.

With the analysis of experimental samples from interrupted softening and melting tests, the interruption procedure (and cooling) must be considered in the interpretation of the results. Of particular importance is recognition of microstructures which may have been generated on cooling. The interruption procedure for the tests involved passive cooling under nitrogen once the target sample temperature had been reached. The passive cooling rate was between 5 °C/minute and 10 °C/minute,[22] resulting in a time to reach 1100 °C (at which point liquid presence is unlikely) of around 30 minutes. As such, detailed micro-analysis of both systems is carefully considered in the context of the cooling procedure.

B. *Slag Analysis*

Polished longitudinal sections from the mixed burden samples (1300 °C) were carbon coated and fitted to a custom SEM stage. The stage allowed the entire section to be scanned intact. A TESCAN Integrated Mineral Analyser (TIMA)[31] was used for SEM-EDS data acquisition. The system employs four EDS detectors to facilitate rapid analysis. Acceleration voltage was 25 keV at a working distance of 15 mm.

Lump ore, being a natural product, can contain a range of particle textures for which the reducibility and chemistry can vary.[32] As such, with the local assessment of interfacial conditions, the various microstructures and compositions that can exist in the lump ore particles must be considered. To identify regions of interest for detailed scanning, a qualitative element map was produced for the entire section. For this scan, a pixel size of 10 μm was used with 1000 X-ray counts collected per pixel. Colored element maps including Mg, O, Si, Al, and Ca (in order of display) were generated using the TIMA software. Fe was excluded from the color maps to allow greater contrast between gangue elements. From this map, as well as the reflected light microscopy images, burden interfaces were generalized into two types—defined by the reduction characteristics of the lump particles. Specifically, lump particles with a high metallization or low metallization in direct contact with sinter were selected for detailed analysis. One example of each of these interfaces was selected under both the Base Case and Hydrogen Case gas.

C. *Mapping of Oxide Properties*

As discussed previously, SEM-EDS mapping and FactSage are both commonly used to study liquid and solid fractions and compositions for individual points or for bulk compositions in softening and melting samples. In this study, a novel integrated approach was developed to plot a map of the calculated thermodynamic output from FactSage onto every point of quantified SEM-EDS maps. For these images, acquisition scans were conducted using the TIMA at 25 keV with a working distance of 15 mm. A pixel size of 4 μm was used (close to practical resolution/interaction volume of beam) with 30,000 X-ray counts collected per pixel. The methodology developed to integrate thermodynamic calculations and EDS maps is described.

Python 3.10 scripts were used to automate quantification of collected spectra within the TIMA software (version 2.8.1). The standardless quantitative analysis tool in the TIMA software was used for all spectra quantification. Carbon was specified as the coating element with the removal of escape peaks and sum peaks. Analysis was performed for Mg, Ca, Fe, Al, Si, and O (all measured), returning normalized atomic percent compositions. The python scripts output tables of compositions assigned a pixel-ID (linearly indexed for image reassembly). MATLAB 2022b was used to reassemble the compositions into quantitative EDS maps and generate Excel files for use in FactSage macro calculations. Pixels comprised of predominantly

Table I. Chemical Composition of Burden Arrangements in Softening and Melting Tests

Material	TFe (Wt Pct)	FeO (Wt Pct)	CaO (Wt Pct)	SiO_2 (Wt Pct)	Al_2O_3 (Wt Pct)	MgO (Wt Pct)	Basicity
NBLL	62.8	—	0.05	3.70	1.4	0.1	0.01
MB1	57.98	6.00	7.94	5.07	1.77	1.41	1.57
SH1	56.70	7.60	10.04	5.43	1.87	1.76	1.85

metallic iron (discerned as compositions with > 80 at pct Fe) were excluded from the output. A FactSage 8.2, Equilibrium Module (FToxid, FactPS) macro was used to automate the calculation of equilibrium phases for each pixel. Equilibrium calculations for each pixel were performed through input of the quantified elemental compositions measured by EDS (*i.e.*, no assignment of stoichiometry was assumed for the oxygen). All solid and solution phases were selected, with duplicates suppressed (priority order FToxid > FactPS). The calculation temperature was specified as the interruption sample temperature of the experiment (1300 °C). The primary outputs from the equilibrium calculation were the amount of liquid slag and solid oxides and their composition. The liquid fraction present at 1300 °C was then calculated. Metallic iron formed in the equilibrium calculation was excluded from determination of liquid and solid fractions, so as to only express the proportions of the oxide phases (in equilibrium with metallic iron). The FactSage macro wrote results back to the input Excel file, which was read by MATLAB 2022b for reassembly into an image.

D. *Average Line Scans*

While the two-dimensional mapping provides a spatial visualization for the properties of the oxide system, preservation of this information may be particularly susceptible to artifacts of microstructures generated on cooling. To combat this, compositions were averaged across lines of pixels perpendicular to the interaction interface. These averaged compositions better reflect a representative composition at a particular distance from the interface.

In addition to averaging possible microstructural artifacts generated during cooling, the line scans provide a one-dimensional representation of the composition changes (and the calculated thermodynamic properties) across the interface. In order to provide additional insights to the produced thermodynamic maps of the oxides, the liquid composition and the metallic iron content were included in the output composition of the line scans.

The line scans were produced using the same data files output by FactSage for the thermodynamic maps, as well as a map of pixels considered to be metallic iron (> 80 at pct Fe) determined by the quantified SEM-EDS maps. In all images, the orientation of the interface (be it vertical or diagonal) was identified. Compositions were then averaged for rows of pixels parallel to the interface. This sequence was repeated, starting at a base coordinate in the lump particle, and ending at the final row of pixels in the sinter. The averaged compositions determined for each row of pixels could then be plotted as a function of distance from the zero point of the imposed coordinates.

E. *Metal Carbon Analysis*

In the previous study,[22] molten metallic iron droplets were observed under the Hydrogen Case gas in the sinter and mixed burdens at 1450 °C, but not lump. This was indicative of differences in carburization behavior between lump ore and sinter. For this reason, carbon content was investigated in individual burdens to allow for direct comparison. Carbon content was inferred in samples interrupted at 1300 °C to determine the carburization of the metal before the formation of liquid. As such there are four conditions in which the presence of carbon was assessed: NBLL under the Base Case gas, NBLL under the Hydrogen Case gas, SH1 under the Base Case gas, and SH1 under the Hydrogen Case gas.

The presence of carbon was inferred using metallographic etching with 2 pct Nital for 20 to 40 s (dependent on sample).[24] Etched samples were imaged at 50× magnification in order to identify grain structures indicative of the carbon concentration (ferrite, pearlite, cementite). With possible uneven gas flow through the ferrous layer, image locations were selected both close to and away from the walls of the graphite crucible. Images were acquired in regions which also did not have direct contact with a carbon source (coke or graphite) to exclude them as a source of carbon (*i.e.*, the carbon in the metal in these regions most likely originated from the gas phase).

1. *Metallographic carbon content qualification*

During reduction of the ferrous burden particles, pure iron crystallizes from the oxide phase into a partitioned network. With the variation in carburization behavior of this iron, at the onset of melting there can exist a network of what is, in essence, a low carbon steel inside the particle. As such, metallographic etching is an appropriate method for qualitative determination of its carbon content.[23,24] For low carbon steels, the primary structure of interest is pearlite (corresponding to 0.8 wt pct carbon), which is identified by its lamellar structure. The proportion of pearlite within a cross sectional area can be used to approximate the carbon content between 0 and 0.8 wt pct carbon (corresponding to 0 to 100 pct pearlite).

III. RESULTS AND DISCUSSION

In the previous study, the authors reported results from individual and mixed burden softening and melting tests with hydrogen addition.[22] The experimentally recorded pressure drop (kPa) and contraction (pct) are reprinted in Figure 1 for completeness. The experimental results presented in Figure 1 represent observed changes to the overall performance of the lump, sinter, and mixed burdens with the introduction of hydrogen. The subsequent analysis aims to determine the metallurgical drivers of these observed changes.

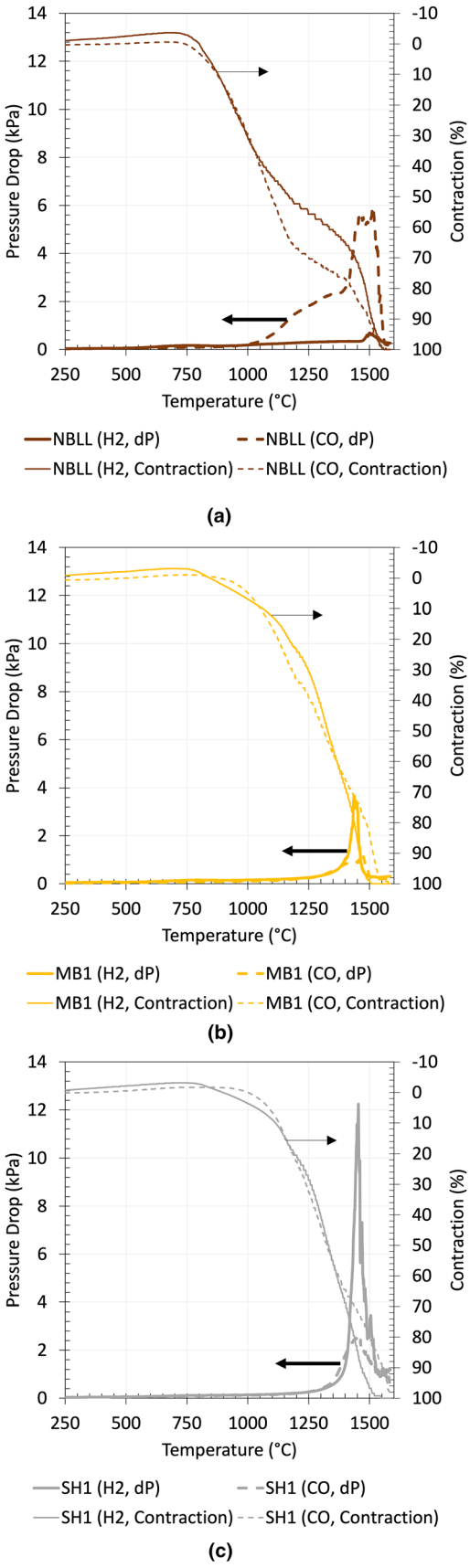

◀Fig. 1—Experimental pressure drop and contraction plotted with sample temperature from previous study for each burden type. Reprinted with permission from Ref. [22]).

Figure 1 demonstrates that with the inclusion of hydrogen (solid line), NBLL (a) pressure drop improves markedly, while SH1 (c) pressure drop is significantly higher. The mixed burden (b) demonstrates the most desirable performance (lower maximum pressure drop than sinter, not sustained for as long as lump), indicating that an interaction still occurred between the dissimilar burdens with the inclusion of hydrogen. The mechanisms of this interaction are explored in the following section.

In the following discussion, the macro-scale qualitative element maps are first shown, with detailed regions of interest indicated. Following this, the quantified SEM-EDS maps of the indicated regions are presented to provide context for the proceeding calculations. Following these element maps, the oxide gangue/slag system is analyzed first, followed by the metallic iron/carbon system. Finally, after the analysis of each system independently at the microscale, considerations for interpretation of results in the (real) mixed system are discussed and related to the observed softening and melting test performance.

A. *Macroscale Element Distribution*

The light optical micrographs of the interrupted samples are shown in Figure 2 and the qualitative element distribution maps (SEM-EDS) are shown in Figure 3. The associated color legend and X-ray scaling is included.

Being such a large image, many interesting macroscale features can be observed from the distribution of elements in Figure 3. Of particular importance is the macro-heterogeneity of elements. Sinter, evidenced by the presence of well-distributed calcium (pink), contains local regions of magnesium (blue) and relict ore particles (un-reduced/yellow regions). Conversely, lump ore particles are relatively homogenous, but differences are evident between individual particles (gangue content/composition, reducibility, and reduction morphology). These characteristics result in the formation of many different microscale interfacial conditions in which liquid may first form and interact with its surrounding material.

As previously discussed, interfacial regions between lump and sinter particles were selected for detailed analysis based on the properties of the lump particle. To reiterate, Figure 3 presents the element map excluding iron so as to allow greater contrast between the gangue/oxide elements. As such, the metallic iron can be inferred from Figure 2 as the brightest (most reflective) regions. Through assessment of both Figures 2 and 3, the lump particles were categorized into high metallization (high brightness particles in Figure 2, dull particles in Figure 3), and low metallization (yellow regions in Figure 3). The selected regions are indicated by the red

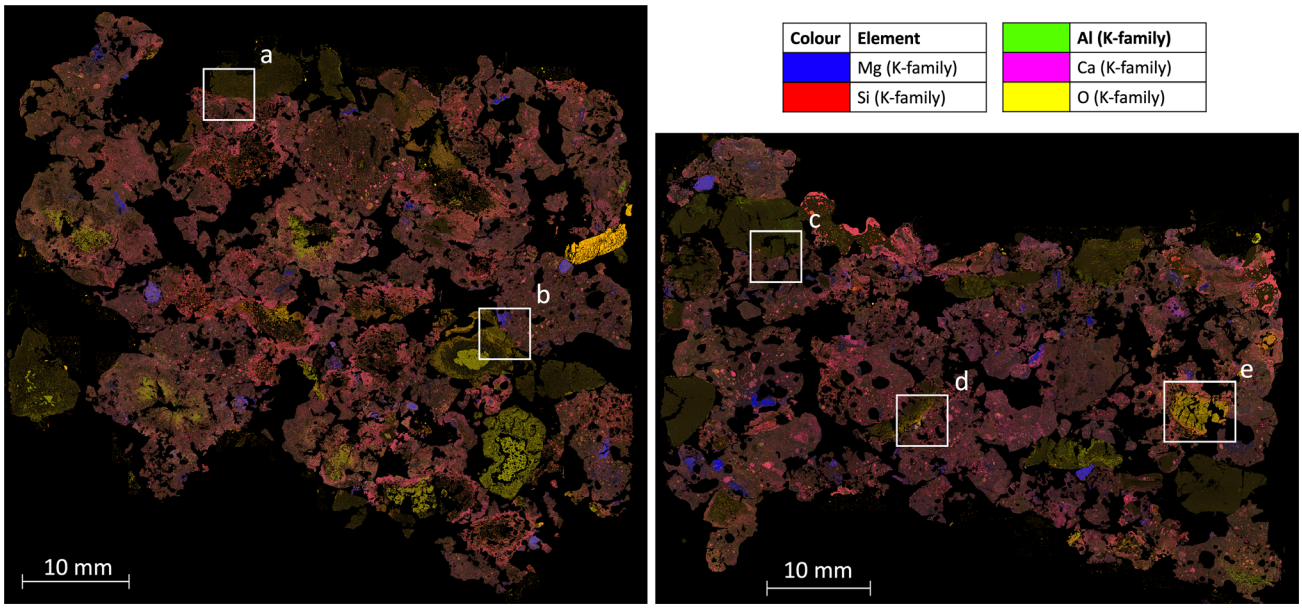

Fig. 2—SEM-EDS element map of entire softening and melting sample cross section at 1300 °C. (Left: MB1 under Base Case gas, Right: MB1 under Hydrogen Case gas. NB. Fe is excluded from the color maps to allow greater contrast between gangue elements).

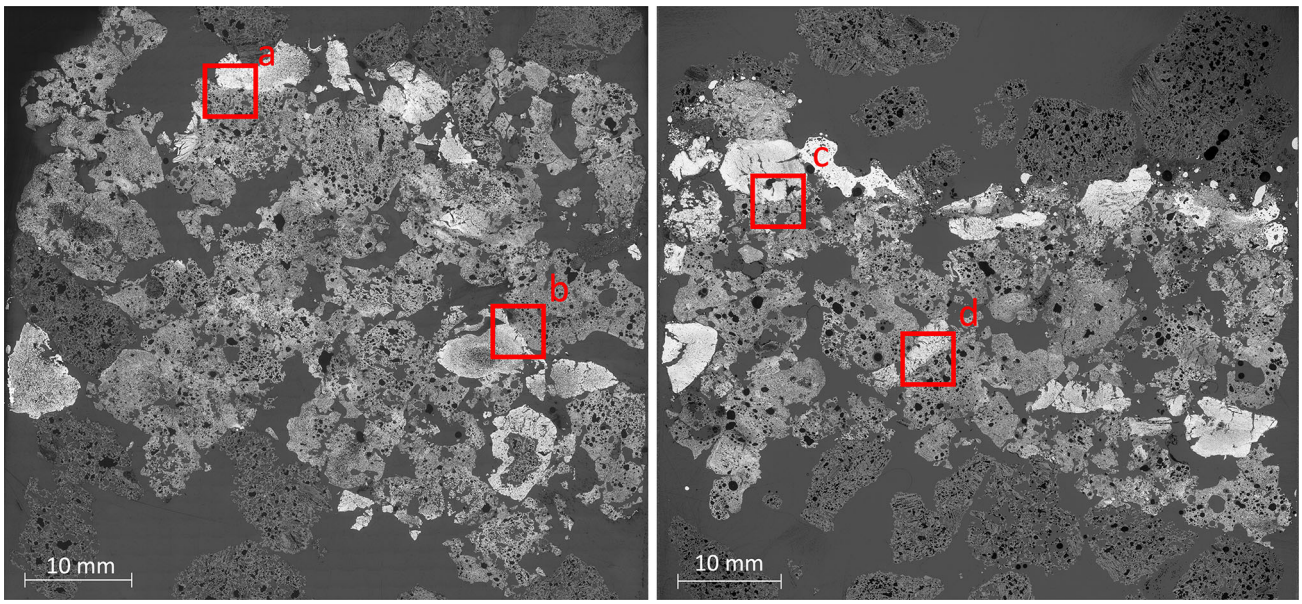

Fig. 3—Light optical microscopy image of entire softening and melting sample cross section at 1300 °C. (Left: MB1 under Base Case gas, Right: MB1 under Hydrogen Case gas).

and white boxes in Figures 2 and 3, respectively. Regions (a) and (b) represent high and low metallization lump particles, respectively, under the Base Case gas. Regions (c) and (d) represent high and low metallization lump particles under the Hydrogen Case gas. It should be noted that the one particle (region (e) in Figure 3) with significantly lower metallization under the Hydrogen Case gas resembles a relict ore particle embodied in sinter. As such, it was excluded from analysis.

It is emphasized that high metallization lump particles existed under both gas conditions, consistent with the inherent reducibility differences between individual lump ore particles. However, overall, the mixed burden under the Hydrogen Case gas contains more highly metallic lump particles than the mixed burden under the Base Case gas. The mixed burden under the Base Case gas also contains lump particles with un-reduced wustite cores (yellow). These characteristics reflect the reduction degree calculated for the single material tests of lump,[22]

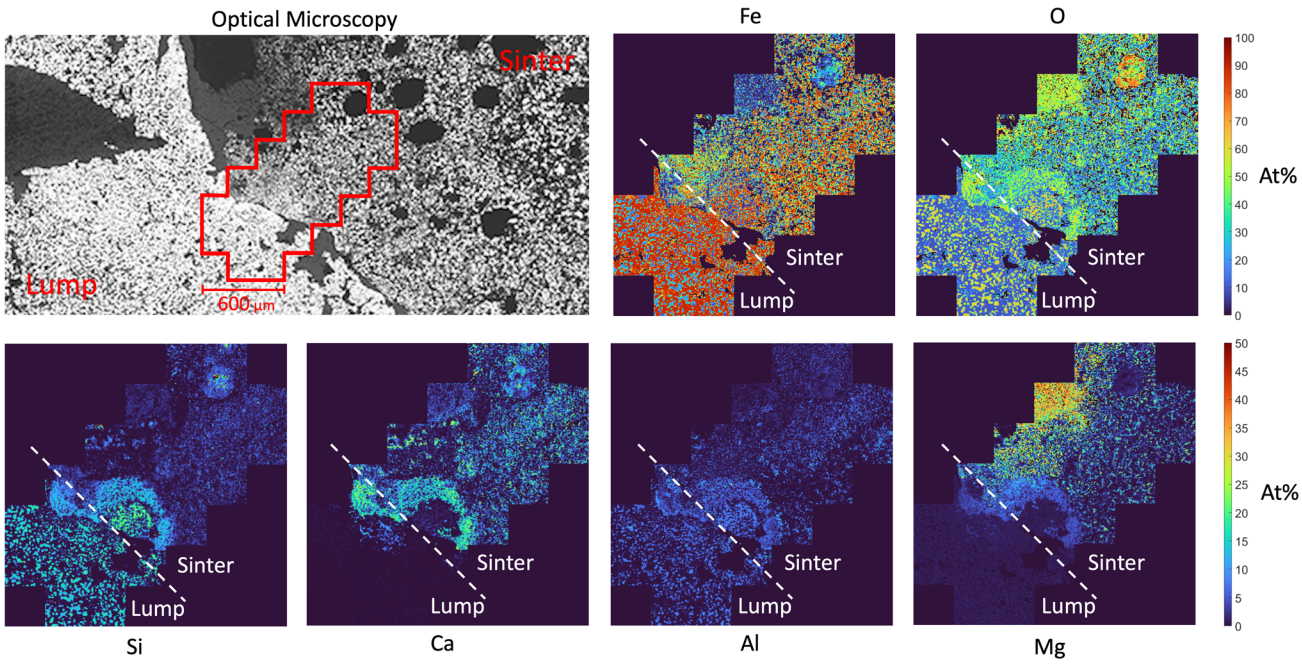

Fig. 4—Quantified SEM-EDS element map for low metallization lump particle in contact with sinter under Base Case gas (corresponding to area (b) in Figs. 2 and 3). Top left image shows broader region as imaged by light optical microscopy (the scanned region is outlined in red for comparison).

which was significantly higher under the Hydrogen Case gas and showed no plateau in reduction (associated with the formation of wustite cores/low-temperature melt formation).[33]

1. *Quantified element maps*

With the assessment of real, local interfaces between the burden types, complexities arise in analysis due to the micro-heterogeneity of the materials, as well as the variations in initial material composition. As such, in order to understand the calculated thermodynamic properties, the measured chemical composition at the identified interfaces must be considered. Figures 4 through 7 show the quantified SEM-EDS element maps for each of the interfaces identified in Figure 3. The top row of images shows iron (Fe) and oxygen (O) on a color scale from 0 to 100 at pct, while the bottom row of images shows silicon (Si), calcium (Ca), aluminum (Al), and magnesium (Mg) on a color scale from 0 to 50 at pct. An approximate interface between the burdens is indicated by the dashed line. It is noted that the real interface and interaction regions are non-linear. These curved regions are indicated later, and explicitly discussed where appropriate.

Figures 4 through 7 demonstrate the distribution of elements within each burden type. The lump side generally contains Si and/or Al, with dense networks of metallic iron. The sinter side generally contains varying amounts of Si, Al, Ca, and Mg, as well as higher concentrations of oxygen associated with the gangue elements. Also demonstrated in Figures 4 through 7 is the micro-heterogeneity of burden materials, consideration of which should be applied to all discussed results. Some key variations in composition occur both between interfaces assessed and within the materials. One example of this is a local region of high magnesium present in the sinter of Figure 4. Variations in the local conditions at the interfaces are a product of both the starting material, and the complex history of the burden up to its interruption in the softening and melting apparatus. As such, while interfaces are assessed from various gas conditions, attribution of the resulting interaction behavior only to the imposed gas conditions is not possible. Instead, consideration of the interaction behavior at low and high degrees of metallization can be applied to macro-scale observations of particle properties.

The composition of the highly metallized lump particles is seen to be different under the gas conditions assessed. Under the Base Case gas (Figure 6), the gangue is primarily silicon based, where under the Hydrogen Case gas (Figure 7) the gangue is primarily aluminum based. These gangue compositions are a product of the initial composition of the lump particles assessed (not the imposed gas conditions). With two different gangue compositions assessed for highly metallic lump particles, a broader range of interaction conditions can be understood.

B. *Slag Interaction Analysis*

In order to present a detailed analysis on the slag interaction, the oxide system is first analyzed independently of the metallic iron through mapping of its thermodynamic properties. Averaged one-dimensional compositions (inclusive of metallic iron) are presented concurrently so as to provide a holistic understanding of the oxide system and its presence in the surrounding

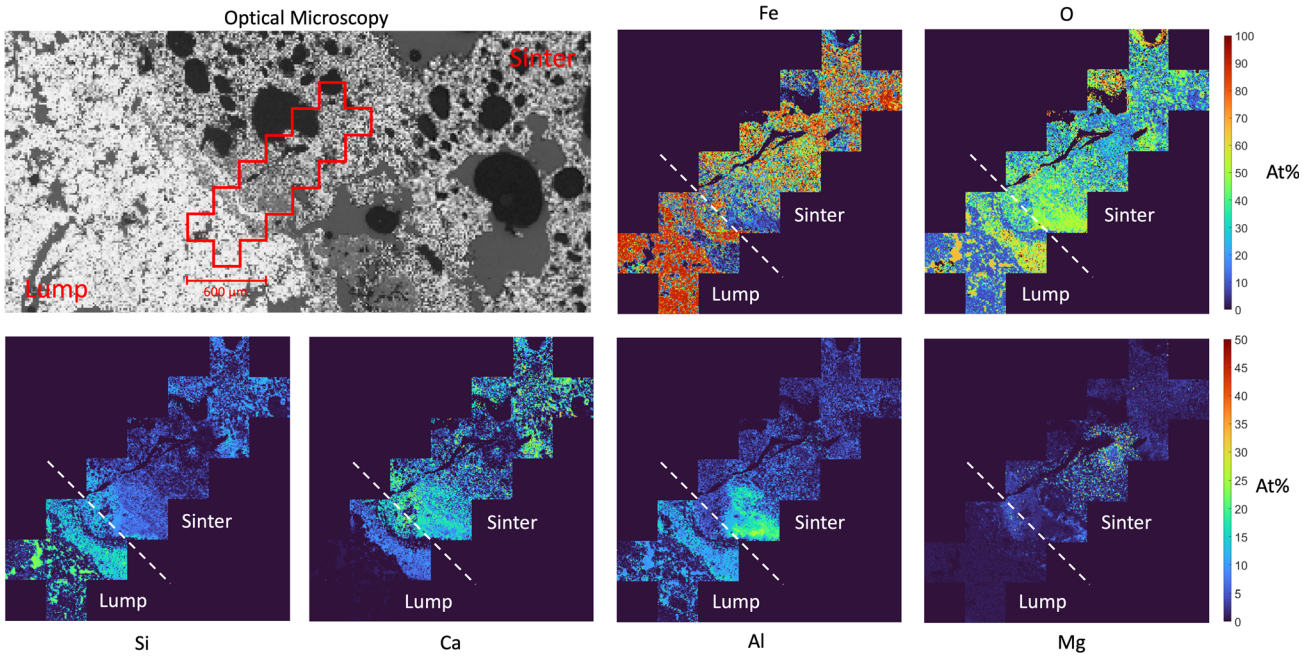

Fig. 5—Quantified SEM-EDS element map for low metallization lump particle in contact with sinter under Hydrogen Case gas (corresponding to area (d) in Figs. 2 and 3). Top left image shows broader region as imaged by light optical microscopy (the scanned region is outlined in red for comparison).

microstructure. Following this, the solid phase stability in equilibrium with the formed oxide slag is analyzed, to elucidate mechanisms by which the liquid stability is altered.

1. *Oxide liquid formation*

Figures 8 through 11(a) show the calculated liquid fraction associated with the elemental compositions presented in Figures 4 through 7, respectively, at 1300 °C. As previously discussed, these areas represent interfaces between lump particles with low (Figures 8 and 9) and high (Figures 10 and 11) metallization in contact with sinter under both the Base Case gas (Figures 8 and 10) and Hydrogen Case gas (Figures 9 and 11). In Figures 8 through 11(a), the interface between the lump and sinter particle is approximately indicated by a solid white line. These interfaces are indicated to aid in discussion and were inferred primarily from the region of highest iron in Figures 4 through 7 (due to the higher iron content of lump than sinter), as well as the macro-scale particle boundaries in Figures 2 and 3. In addition to the solid white lines marking the approximate interface, a linear dotted white line is included as a reference position for comparison with the one-dimensional compositions. To reiterate, the liquid fraction (indicated by color) in Figures 8 through 11(a) expresses only the proportion of oxide that is liquid (i.e., all metallic iron is excluded). Background pixels are presented in black (including voids and metallic iron as discerned from SEM-EDS maps).

Figures 8 through 11(b) show the average (one-dimensional) composition in the direction normal to the marked interface (dotted line). The two key additional insights from Figures 8 through 11(b) are the liquid phase composition (represented by the colored bars) and the quantity of metallic iron in which the oxide system resides (represented by the gray bars). As previously described, these compositions included the metallic iron, both as measured from the SEM-EDS maps (defined as > 80 at pct Fe) as well as the metallic iron portion calculated by FactSage. The base coordinate (zero point) is indicated in Figures 8 through 11(a) by the white arrow marked with a zero (top right of Figures 10 and 11, bottom left of Figures 8 and 9). Compositions are represented as a function of distance from this point in the direction of the arrow.

Figures 8 through 11(a) offer a spatial visualization of the proportion of the oxide that is liquid for each interfacial condition, and Figures 8 through 11(b) provide context to the amount of oxide/metal, as well as the liquid composition. As previously stated, with the local assessment of interfaces, the properties of both the lump and sinter burden determined in Figures 8 through 11 are a product of the (varying) starting materials at the interface and a complex, non-isothermal reduction history. Because of this, interpretation of these results is largely restricted to the comparison of interaction behavior between sinter and lump particles with low or high metallization. This comparison is in the context that, as per Figures 2 and 3, there were significantly more lump particles with high metallization under the Hydrogen Case gas than the Base Case gas.

From Figures 8 through 11(a), the sinter behavior away from the interfaces is relatively consistent, characterized by ~ 40 to 50 wt pct oxide distributed in a uniform network. Of this oxide, from Figures 8 through 11(b), ~ 40 to 60 wt pct is liquid, which is predominantly composed of FeO, CaO, and SiO_2. Local variations in

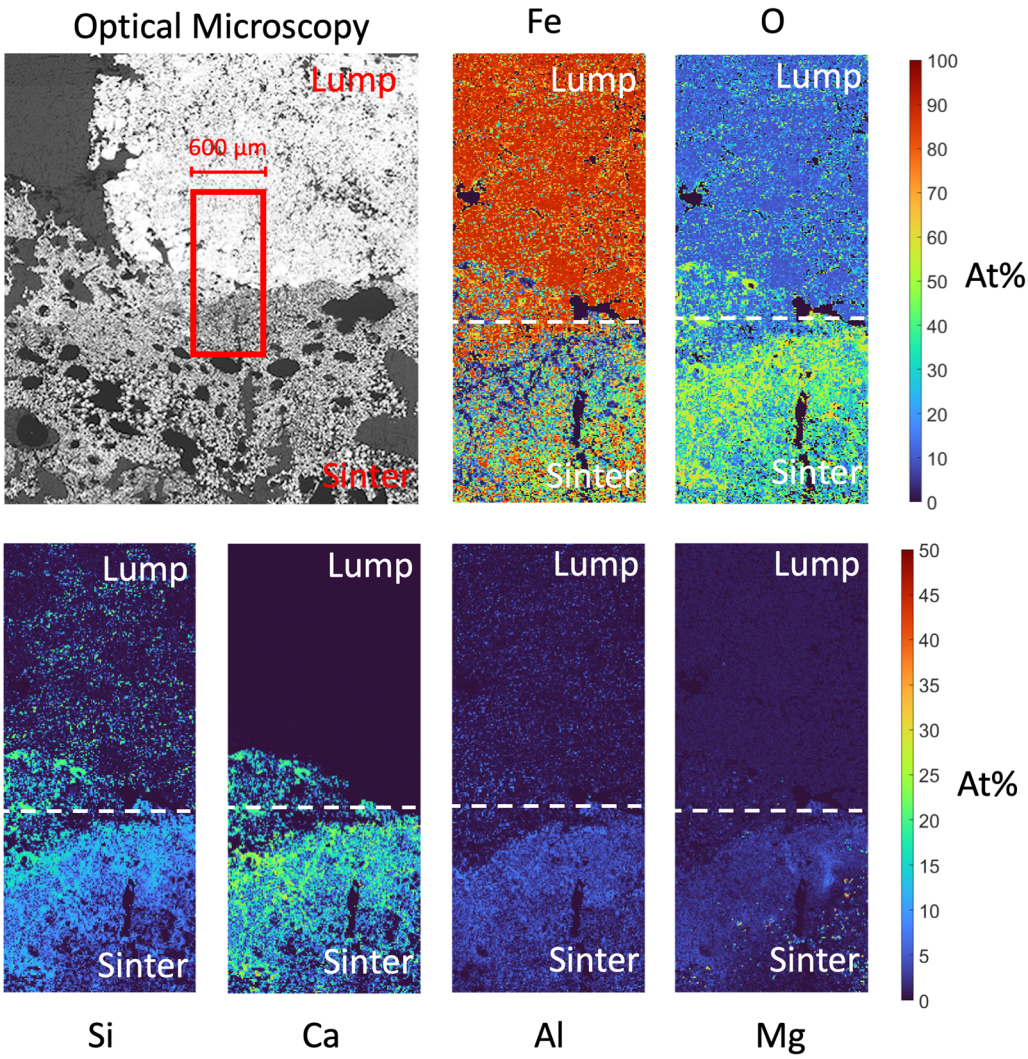

Fig. 6—Quantified SEM-EDS element map for high metallization lump particle in contact with sinter under Base Case gas (corresponding to area (a) in Figs. 2 and 3). Top left image shows broader region as imaged by light optical microscopy (the scanned region is outlined in red for comparison).

composition are evident from the element maps (Figures 4 through 7) and are seen to directly impact the liquid formation behavior within the sinter. One example of this is the regions of high magnesium in Figures 4 and 7 which directly correlate with regions of lower liquid fraction in Figures 8(a) and 11(a), respectively.

For lump particles away from the interfaces, the amount of oxide is generally lower than that of sinter, as evidenced by the magnitude of colored and white bars in Figures 8 through 11(b). Low metallization lump particles are also seen to contain significantly more oxide, with ~ 30 to 40 wt pct compared to ~ 10 wt pct for highly metallized lump particles. The spatial sparsity of oxide in highly metallic lump particles observed in Figures 10(a) and 11(a) is also reflective of the lower total oxide content seen in Figures 10(b) and 11(b). For all lump particles, the liquid is primarily composed of FeO and SiO_2. However, unlike the uniform network of partially molten oxide observed for sinter, liquid and solid phases are generally partitioned from each other, with some regions fully liquid, and others almost fully solid. Of note, the highly metallized lump particles show different liquid formation behavior. While in both particles there is ~ 10 wt pct oxide remaining, the oxide of the highly metallized lump particle under the Hydrogen Case gas (Figure 11) generated significantly less liquid than that of the Base Case gas (Figure 10). The impact of the composition of the parent lump particles on this liquid formation will be discussed later, with consideration of the solid phase stability.

The most interesting behavior occurs around the interfaces between the dissimilar burdens, approximately indicated by the white freeform line in Figures 8 through 11. For the low metallization interface under the Base Case gas (Figure 8), a curved region of suppressed liquid formation (blue) resides close to the interface, within the sinter. Similarly, for the low metallization particle under the Hydrogen Case gas

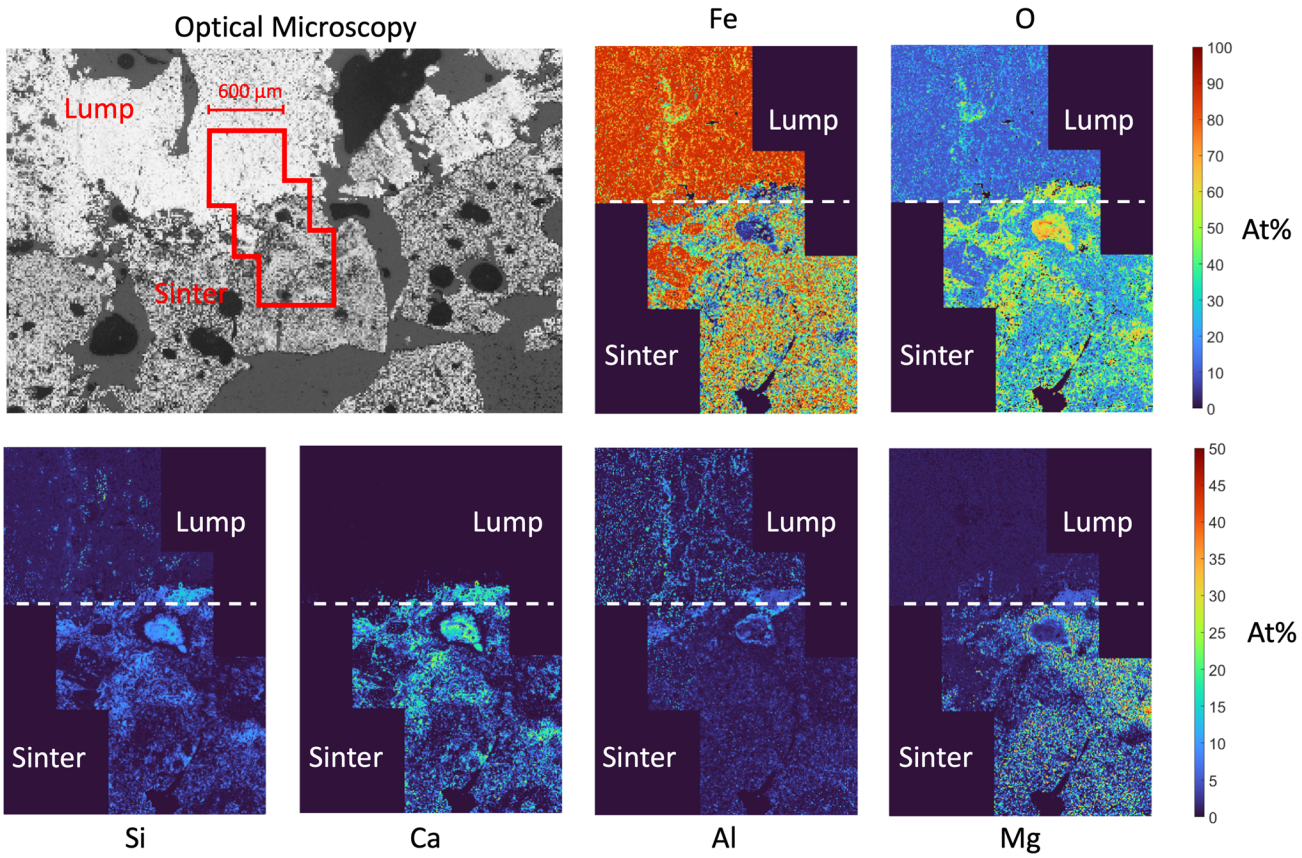

Fig. 7—Quantified SEM-EDS element map for high metallization lump particle in contact with sinter under Hydrogen Case gas (corresponding to area (c) in Figs. 2 and 3). Top left image shows broader region as imaged by light optical microscopy (the scanned region is outlined in red for comparison).

(Figure 9), a band exists around the interface with significantly lower liquid oxide fraction than the bulk materials (blue color). Within these regions, primary slags from the lump ore and sinter have interacted to form new phases, which are evidently more stable at the specified temperature. Artifacts of the interaction dynamics can also be observed in the low metallization particles. Under the Base Case gas, the reaction front has moved from the lump into the sinter, with the entire region of suppressed liquid formation residing in the sinter. Under the Hydrogen Case gas, the reaction band is wider, and a region of suppressed liquid formation is present in both the sinter and lump regions. Interestingly, the liquid phase around the interface of the low metallization lump particles (Figures 8 and 9) contains CaO, however, is generally devoid of MgO.

With the highly metallized lump particles showing comparatively different liquid formation, the interaction behavior also changes. The highly metallized lump particle under the Base Case gas (Figure 10) demonstrates particularly interesting behavior, as it is an example of a highly metallized particle which has formed liquid (and proceeded to interact). Conversely, under the Hydrogen Case gas (Figure 11) both the lump and sinter contain a low mass fraction of liquid. Because of the complexity of the starting materials and reduction history, these differences cannot be attributed only to the gas conditions. The results do indicate, however, that an interaction can occur at a high level of metallization. This is seen under the Base Case gas in Figure 10, where a region at the interface contains significantly lower liquid fraction than the burdens on either side. Additionally, it can be seen from the interface under the Hydrogen Case gas (Figure 11) that the oxides (which are primarily solid) only have an extremely narrow band of interaction occurring directly at the interface. These results are consistent with the previous suggestions that the interaction is primarily facilitated by the liquid phase,[3,9] which holds true at high degrees of reduction.

Figures 8 through 11 demonstrate the change in liquid formation characteristics of oxide in the bulk material (lump and sinter) and at the interaction boundaries. The changes in liquid formation of the interacted slags reflect the observed softening and melting performance of the mixed burdens, compared with that of the individual tested burdens. To summarize, it is demonstrated by Figures 8 through 11 that for low metallization lump particles contacting sinter, liquid formation is suppressed at the interaction boundary between the burdens. For high metallization particles, two separate behaviors are observed. Under the Base Case gas, despite the sparsity of the oxide phase (from the high degree of reduction), considerable amounts of liquid are

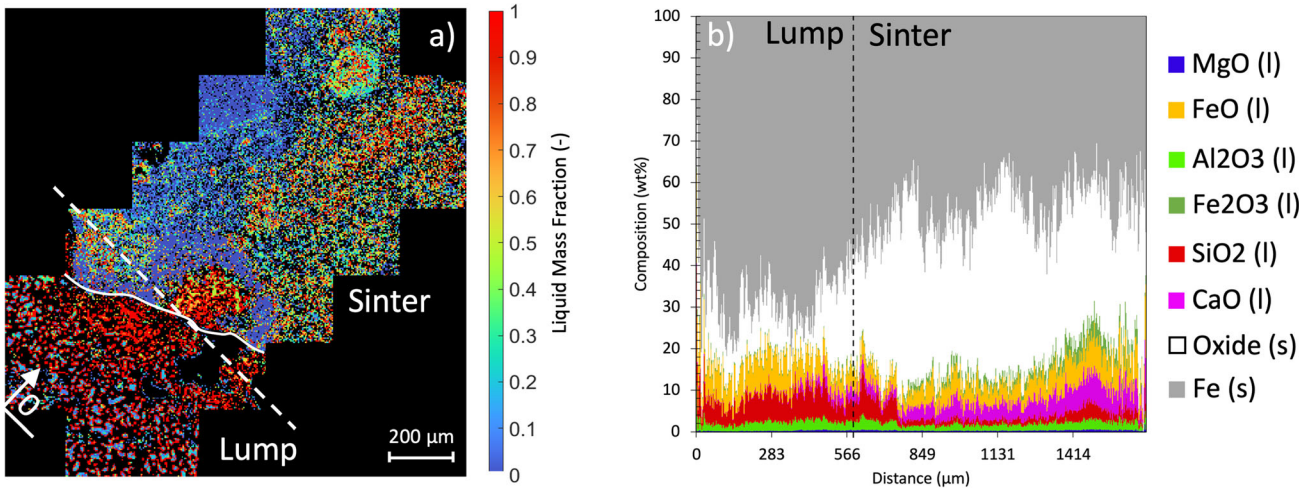

Fig. 8—Liquid formation characteristics of low metallization interface under Base Case gas as calculated by FactSage using SEM-EDS data from Fig. 4. (*a*) Spatial distribution of liquid mass fraction (normalized only to oxide phase). (*b*) Averaged one-dimensional composition including metallic iron.

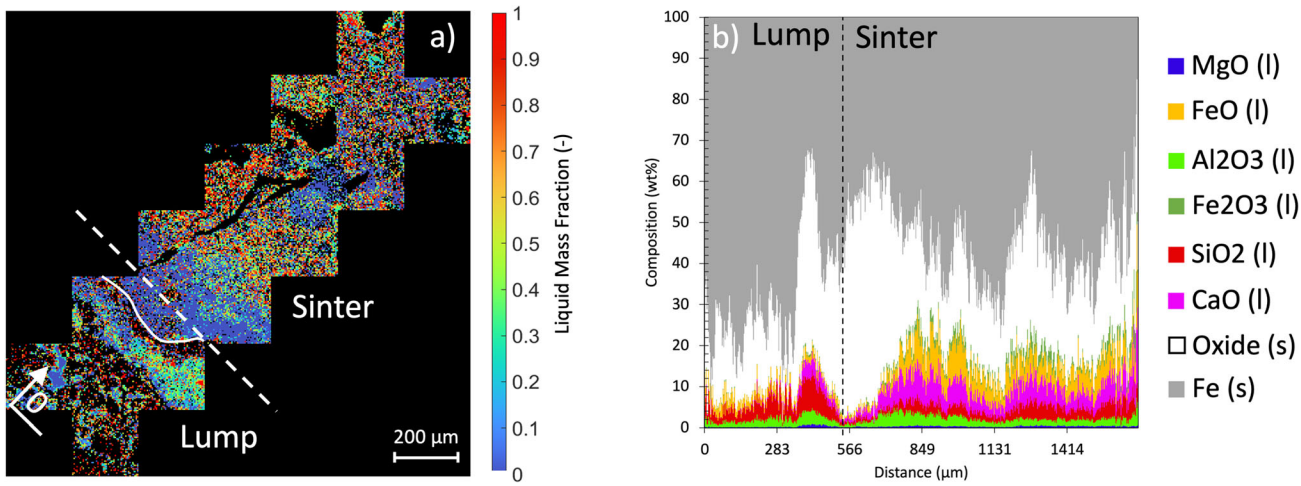

Fig. 9—Liquid formation characteristics of low metallization interface under Hydrogen Case gas as calculated by FactSage using SEM-EDS data from Fig. 5. (*a*) Spatial distribution of liquid mass fraction (normalized only to oxide phase). (*b*) Averaged one-dimensional composition including metallic iron.

formed in both burdens, however, the liquid fraction is suppressed at the interaction boundary between them. Under the Hydrogen Case gas, little liquid is observed in either burden and thus a marginal region of interaction occurred. The suppression of low-temperature liquid phases by means of interaction between the slag phases of the lump and sinter is consistent with the observed improvement of mixed burdens compared with their individual components.[22]

2. *Solid oxide phase composition*

While the liquid formation characteristics can be used to explain the performance improvement of mixed burdens, the solid oxide phases must be considered to determine the mechanisms by which the liquid oxide is suppressed. For this purpose, the solid phases in equilibrium with the generated liquid in Figures 8 through 11(a) are mapped in Figures 12 through 15, respectively. It should be noted that as in Figures 8 through 11(a), these compositions are normalized to only the oxide phases (including liquid oxide), and thus exclude metallic iron. The solid phases reported in Figures 12 through 15 express the short-range order (structural arrangement) of the atoms within the composition range. As such, for many reported mineral phases a range of lattice substitutions can occur. The nominal compositions (be it stoichiometric or with substitution) of the mineralogical names presented in Figures 12 through 15 are shown in Table II.

Where interacted slags demonstrated suppressed liquid formation in Figures 8 through 11(a), the products of the interaction can be observed in Figures 12 through 15. These products are indicative of the mechanisms by which interaction of the liquid with its surrounding

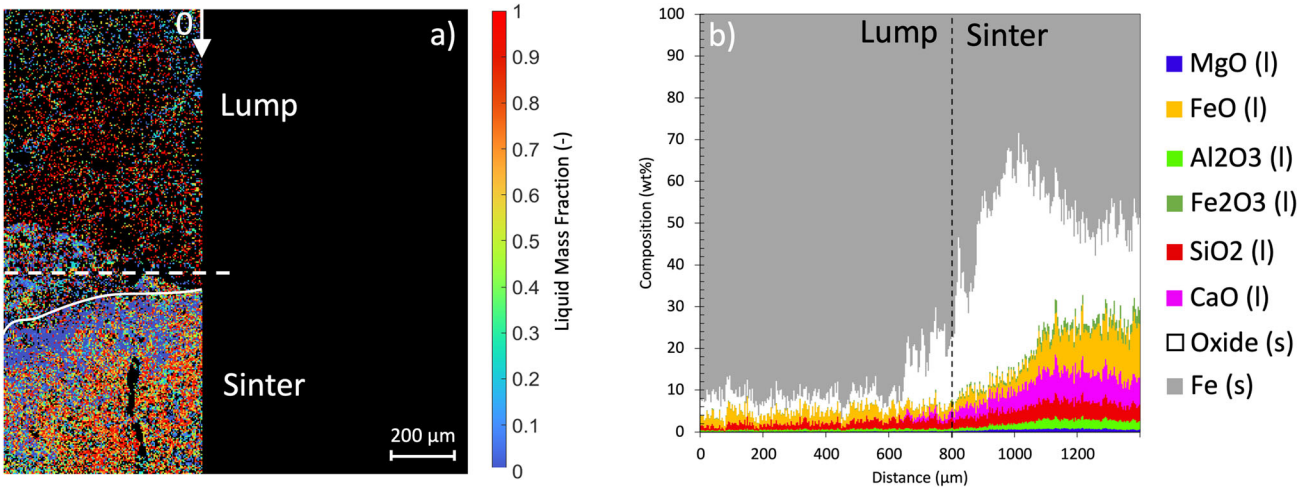

Fig. 10—Liquid formation characteristics of high metallization interface under Base Case gas as calculated by FactSage using SEM-EDS data from Fig. 6. (*a*) Spatial distribution of liquid mass fraction (normalized only to oxide phase). (*b*) Averaged one-dimensional composition including metallic iron.

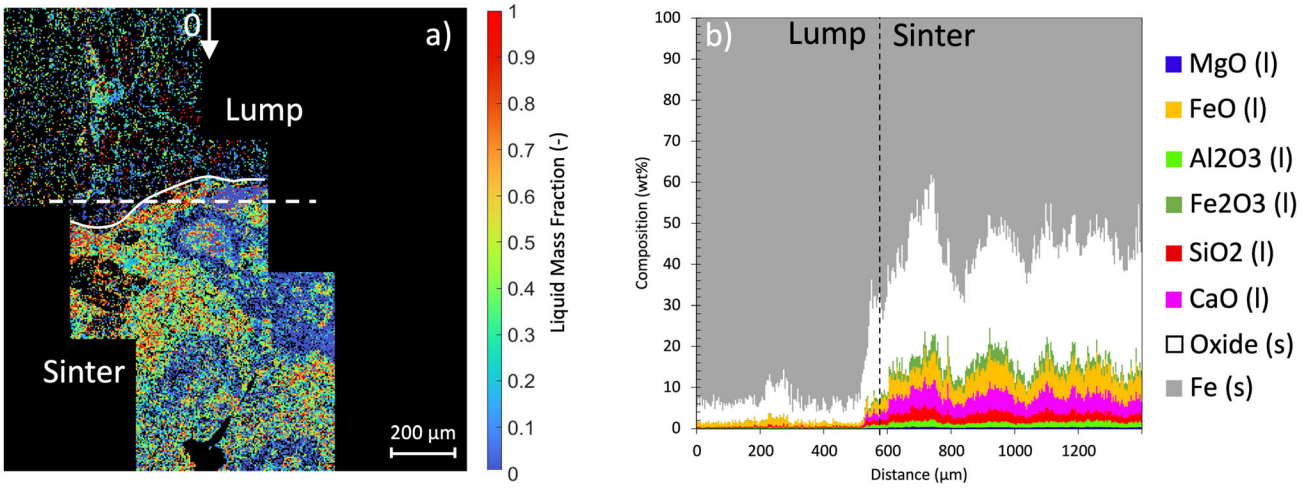

Fig. 11—Liquid formation characteristics of high metallization interface under Hydrogen Case gas as calculated by FactSage using SEM-EDS data from Fig. 7. (*a*) Spatial distribution of liquid mass fraction (normalized only to oxide phase). (*b*) Averaged one-dimensional composition including metallic iron.

material destabilizes the liquid phase. With the variation in initial particle composition and micro-heterogeneity of the assessed interfaces, each interface is analyzed in detail.

For the low metallization lump particle under the Base Case gas (Figure 12), the solid gangue phases are primarily silica based, with some alumina phases present (spinel, mullite)—reflective of the initial gangue composition of the lump particle (see Figure 4). As observed in Figure 8, a significant portion of the lump particle oxide is liquid, composed primarily of FeO and SiO_2. On the sinter side of the interface, the curved region of suppressed liquid (blue in Figure 8(a)) directly correlates with a curved region of unique mineral formation in Figure 12. The presence of these minerals (and lower liquid presence) within the sinter region implies the migration of lump liquids into the sinter, which after interaction with the MgO-rich region of sinter have re-solidified. With the local region of magnesium close to the interface under the Base Case gas (see Figure 4), solid phases are formed which either contain stoichiometric magnesium or allow magnesium substitution into the lattice. These minerals are bredigite, merwinite, melilite, and olivine, many of which have been previously identified as products of the interaction under traditional conditions.[7] Additionally, larnite (also called dicalcium silicate) is seen to exist within this interaction band.

For the low metallization lump particle under the Hydrogen Case gas (Figure 12), the solid gangue phases are primarily silica and mullite—again inherited from the initial particle composition (see Figure 5). The sinter composition at this interface was largely devoid of MgO (Figure 5), with a significant amount of the oxide

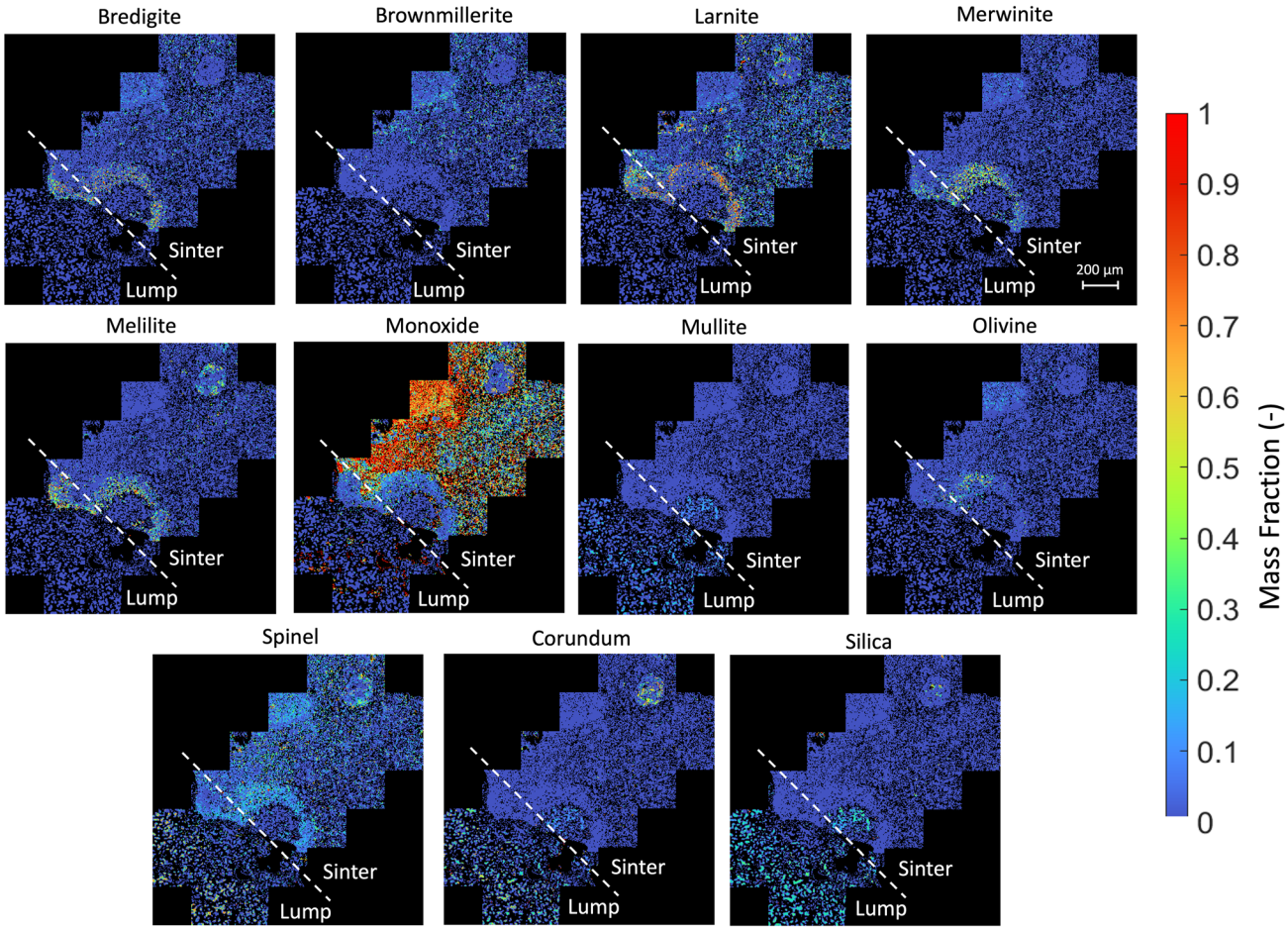

Fig. 12—Spatial distribution of solid phases at low metallization interface under Base Case gas as calculated by FactSage using SEM-EDS data from Fig. 4. Color indicates mass fraction normalized only to oxide (including liquid presented in Fig. 8).

Table II. Mineral Phase Names and Nominal Compositions

Mineral Name	Nominal Composition
Anorthite	$CaAl_2Si_2O_8$
Bredigite	$Ca_7MgSi_4O_{16}$, $Ca_3Mg_5Si_4O_{16}$
Brownmillerite	$Ca_2(Al,Fe)_2O_5$
CAF	$Ca(Al,Fe)_2O_4$
Cordierite	$Al_4(Mg,Fe)_2Si_5O_{18}$
Corundum	Al_2O_3, Fe_2O_3
Larnite	Ca_2SiO_4
Melilite	$Ca_2(Mg,Fe)Si_2O_7$
Merwinite	$Ca_3MgSi_2O_8$
Monoxide	CaO, MgO, FeO
Mullite	Al_4SiO_8, $Al_6Si_2O_{13}$
Olivine	$(Ca,Mg,Fe)_2SiO_4$
Rankinite	$Ca_3Si_2O_7$
Silica	SiO_2
Spinel	$(Mg,Fe)Al_2O_4$
Wollastonite	$(Ca,Fe)SiO_3$

reporting to the liquid phase (Figure 9). Around the interface between the two particles, the region of lowest liquid formation (residing within the sinter in Figure 9(a)) is associated with the presence of larnite and CAF. On the lump side of the interface, a region of anorthite is present (Figure 13). As was seen from Figure 9(b), the liquid composition of the sinter was predominantly FeO and CaO based, with some SiO_2, while the lump was primarily SiO_2 based, with some Al_2O_3. Across the boundary between the particles, a gradient of mineral phases exists from SiO_2/Al_2O_3 rich (lump side) to CaO rich (sinter side). That is to say, with mixing of these liquids at the interface, migration of calcium from the sinter into the lump stabilizes the anorthite phase, while incorporation of SiO_2 and Al_2O_3 from the lump liquids stabilizes larnite and CAF within the sinter.

Through comparison of the low metallization particles (Figures 12 and 13), it can be deduced that the local presence of magnesium has a significant impact on the interaction between the burdens. In both cases, MgO was not observed to participate considerably in the sinter primary slags. However, with the movement of lump primary slags into MgO-containing sinter regions (Figure 12), the liquids were strongly suppressed. Conversely, where MgO was not present under the Hydrogen Case gas (Figure 13), calcium-containing minerals were present on both sides of the interface, with some remaining in the liquid phase at 1300 °C. As

such, while MgO may be more effective at suppressing low-temperature liquids, the CaO may be more mobile (with some being in the liquid phase).

The high metallization lump particles again offer two unique conditions for assessment of interaction mechanisms. As seen in Figures 6 and 7, the initial gangue composition of the lump particles differed. This is also reflected in their solid oxide phase composition, which under the Base Case gas (Figure 14) is primarily silica (SiO_2), and for the Hydrogen Case gas (Figure 15) is mainly spinel ($FeAl_2O_4$). While little liquid was formed under the Hydrogen Case gas, the small interaction region directly at the interface shows unique mineral phases not seen in the bulk burdens. The sinter at this interface contained a relatively high concentration of magnesium, and as such the produced minerals are similar to those of the low metallization particle under the Base Case gas condition (merwinite, melilite, bredigite).

The high metallization interface under the Base Case gas condition shows different solid phase interaction products to those previously discussed. As mentioned, the primary solid gangue phase in the lump particle was silica, and the remaining oxide contained a significant portion of SiO_2/FeO-based liquid (Figure 10(b)). The sinter at this interface contained little MgO (Figure 6), with a significant portion of the remaining oxide present as a FeO/CaO-rich liquid (Figure 10). It is worth noting that with the high metallization of the lump particle, the sinter contained significantly more oxide overall (Figure 10(b)). At the interface between the two burdens, within the sinter (see marked interface in Figure 10(a)), the primary solid phases are melilite and larnite. Within the lump, a gradient of calcium containing minerals is seen moving away from the interface. Specifically, the primary products of interaction are seen to be rankinite and wollastonite. The presence of these calcium containing species within the lump indicates that the sinter liquids have migrated into the lump. The gradient resulting from this migration can be seen in the stoichiometry of the solid compounds observed in this region. On the sinter side of the interface, the composition is primarily that of larnite, a stoichiometric compound with a ratio of 2:1 (Ca:Si). Closest to this interface, within the interaction boundary the presence of rankinite begins, with a stoichiometric ratio of 1.5:1 (Ca:Si), and within the lump region of the interaction boundary, wollastonite appears, which can exist at or below (with lattice substitution) 1:1 (Ca:Si). As such, it can be inferred that the region of suppressed liquid formation in Figure 10(a) is due to the migration of

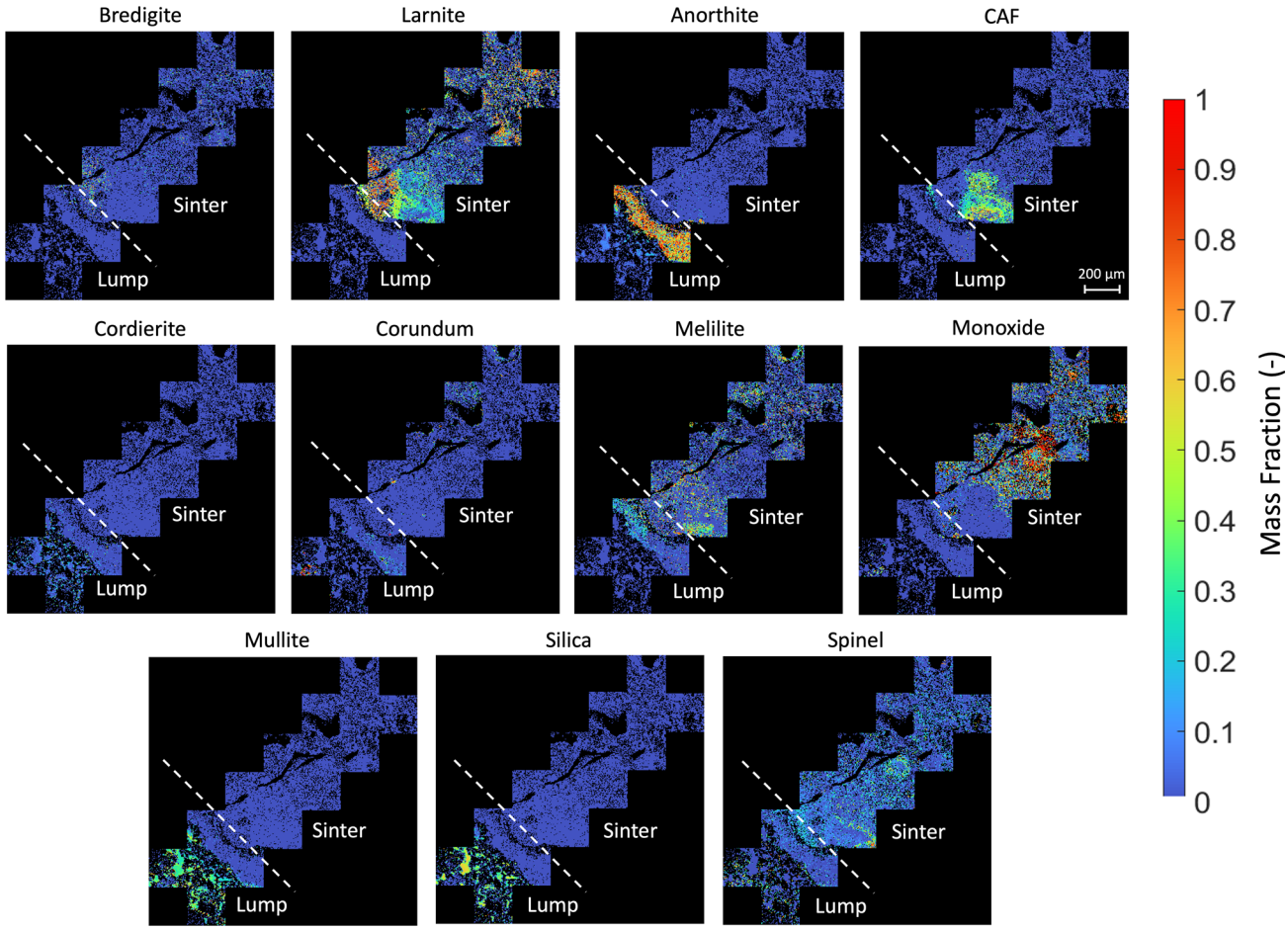

Fig. 13—Spatial distribution of solid phases at low metallization interface under Hydrogen Case gas as calculated by FactSage using SEM-EDS data from Fig. 5. Color indicates mass fraction normalized only to oxide (including liquid presented in Fig. 9).

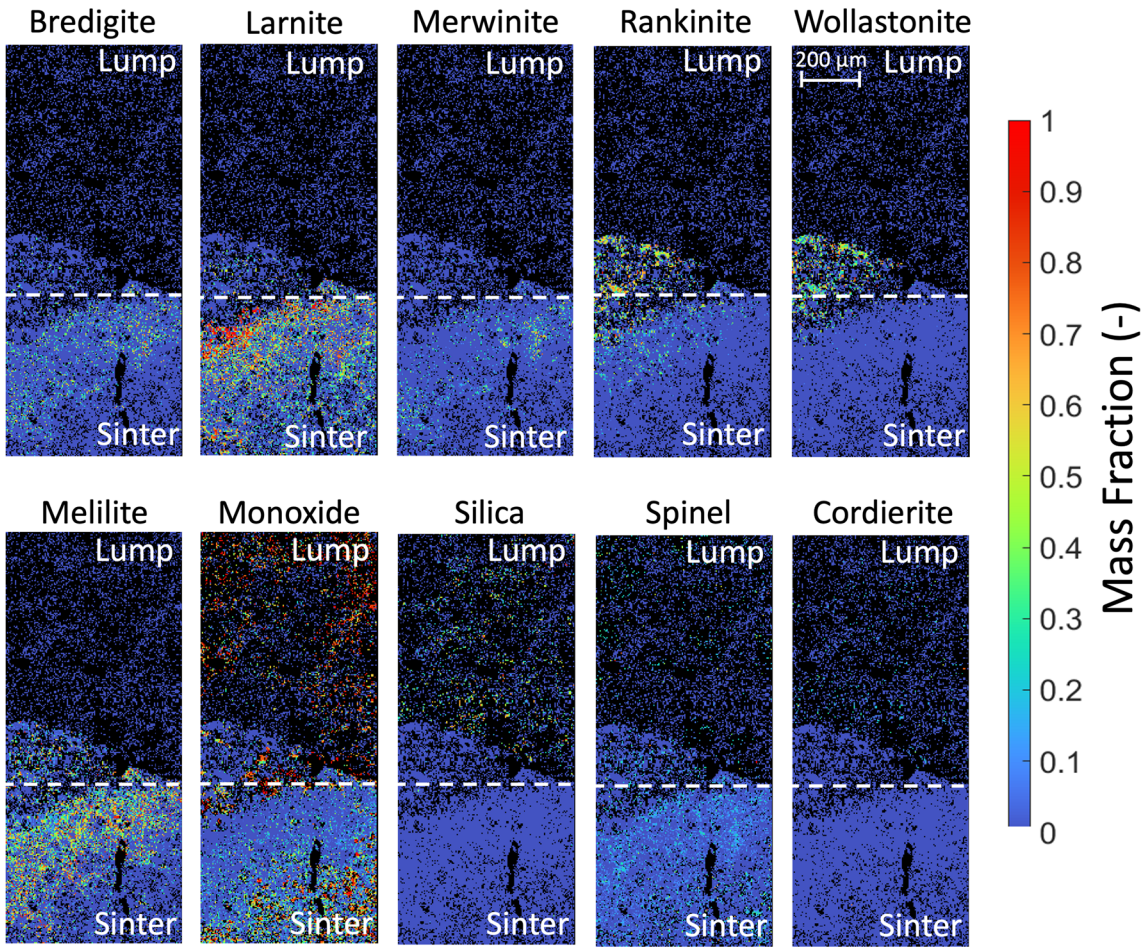

Fig. 14—Spatial distribution of solid phases at high metallization interface under Base Case gas as calculated by FactSage using SEM-EDS data from Fig. 6. Color indicates mass fraction normalized only to oxide (including liquid presented in Fig. 10).

sinter primary slags (CaO rich) into the lump particle, which are re-solidified as calcium silicates by the presence of excess silica in the lump.

C. *Metal Carburization Analysis*

Metal carburization can occur through many pathways, depending on the local conditions present. While metallic iron can be carburized through direct contact with coke (or through a slag layer),[20] gas carburization can occur through dissociation of CO on metallic iron.[17,19] The introduction of hydrogen is known to aid in the removal of desorbed oxygen, and thus increases the rate of gas carburization where oxygen removal is rate limiting.[17,19]

Reflected light microscopy images of the entire sections for the Base Case gas are shown in Figure 16, and the Hydrogen Case gas in Figure 17. In Figure 16, points (a) and (d) represent particles in the central regions for NBLL and SH1 burdens, respectively. Points (b) and (c) represent particles in the wall regions for NBLL and SH1 burdens, respectively. In Figure 17, points (b) and (d) represent particles in the central regions for NBLL and SH1, respectively. Points (a) and (c) represent particles in the wall regions for NBLL and SH1, respectively.

As previously described, sections of individual burdens under both the Base Case and Hydrogen Case gas conditions were etched with 2 pct Nital and imaged at 50x magnification. Two images were taken for each burden under each gas condition, representing regions close to and away from the walls. All regions were selected away from direct contact with coke to ensure the most likely source of carbon was from the gas phase. Figure 18 shows NBLL (top) and SH1 (bottom) under the Base Case gas. Figure 19 shows NBLL (top) and SH1 (bottom) under the Hydrogen Case gas. The corresponding image locations are indicated in Figures 16 and 17, respectively.

In Figures 18 and 19, metallic iron (ferrite) is indicated by the brightest (white) regions. Under the Base Case gas (Figure 18), only ferrite is present, indicating that no carbon was present in the metallic iron for either burden. Under the Hydrogen Case gas, the presence of carbon is indicated by the pearlite structures (P in Figure 19). SH1 under the Hydrogen Case gas (Figure 19) contained ~ 0.08 wt pct carbon (~ 10 pct pearlite) near the wall (c) and ~ 0.4 wt pct

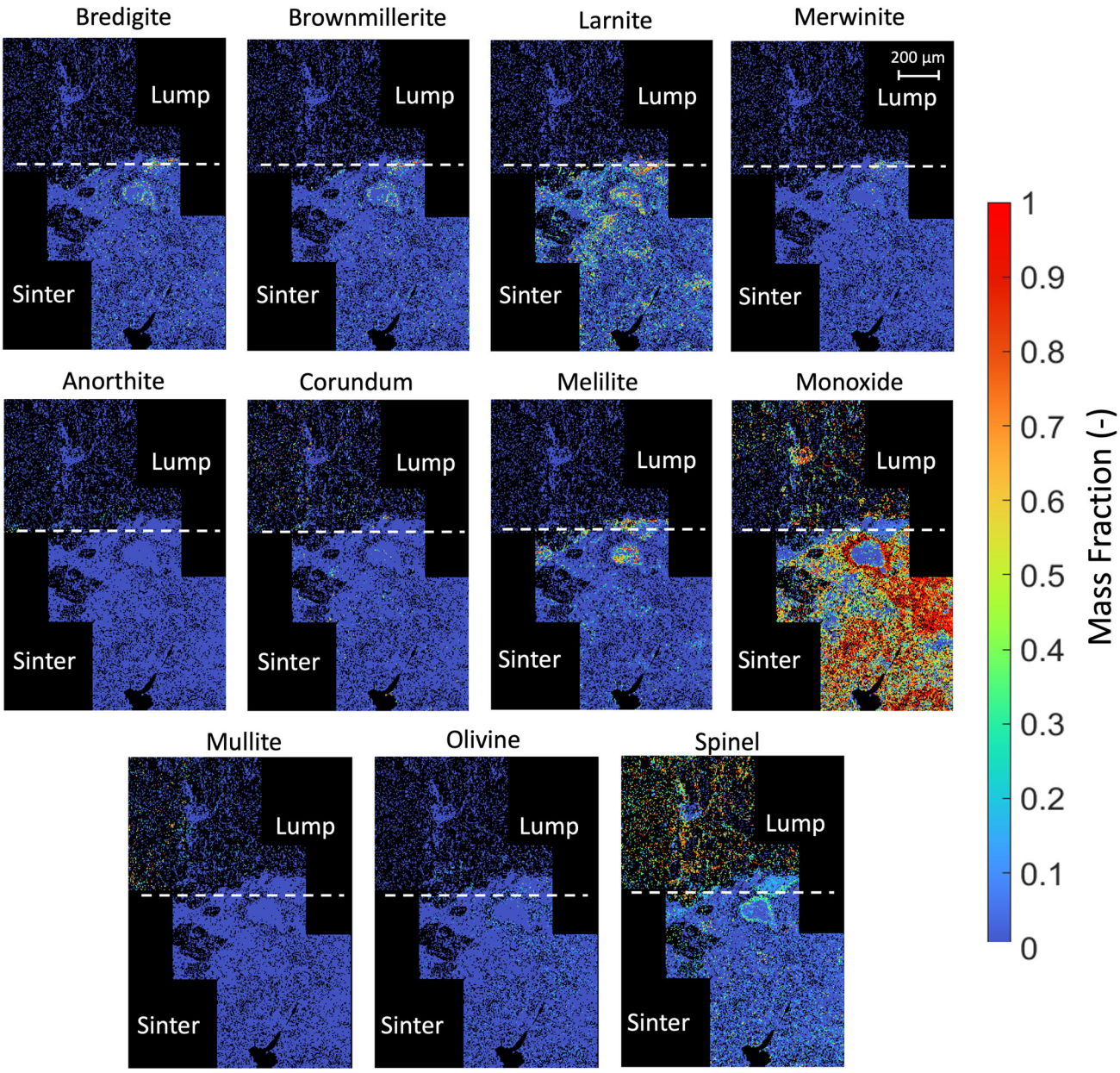

Fig. 15—Spatial distribution of solid phases at high metallization interface under Hydrogen Case gas as calculated by FactSage using SEM-EDS data from Fig. 7. Color indicates mass fraction normalized only to oxide (including liquid presented in Fig. 11).

carbon (~ 50 pct pearlite) in the center (d). Conversely, the bulk of the NBLL burden contained no carbon, consisting only of ferrite (as in image a). However, interestingly one single NBLL particle in the sectioned image contained ~0.08 wt pct carbon (~ 10 pct pearlite) spread throughout (image b). Despite the small amount of carbon in the one NBLL particle, no distinguishing differences were observed from other NBLL particles.

Through comparison of SH1 under the Base Case and Hydrogen Case gas, it can be concluded that the addition of hydrogen did promote the gas carburization of metallic iron for sinter burden. By reference of the Fe-C phase diagram (Figure 20), the carbon content between 0.08 to 0.4 wt pct corresponds to a first liquid formation temperature of 1498 °C to 1446 °C, respectively.

This is consistent with the previously observed physical structures, which showed molten metallic droplets at 1450 °C. While the dynamic behavior between 1300 °C and 1450 °C cannot be directly observed, with the presence of large amounts of molten metallic iron by 1450 °C, it is likely that gas carburization of the metallic iron continued until the onset of melting. The results indicate, however, that sufficient carbon had entered the metallic phase well before the onset of melting, likely through gas carburization. The lowering of the melting

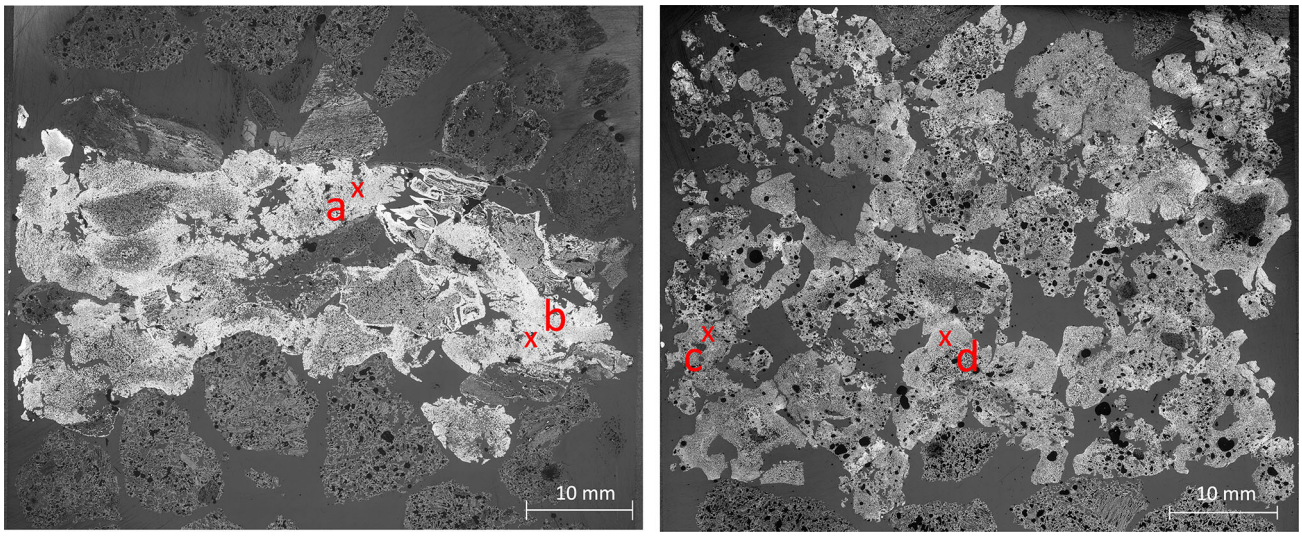

Fig. 16—Reflected light microscopy images of entire softening and melting sample sections under Base Case gas. Left: NBLL ((*a*) central particle, (*b*) wall particle), Right: SH1 ((*c*) wall particle, (*d*) central particle).

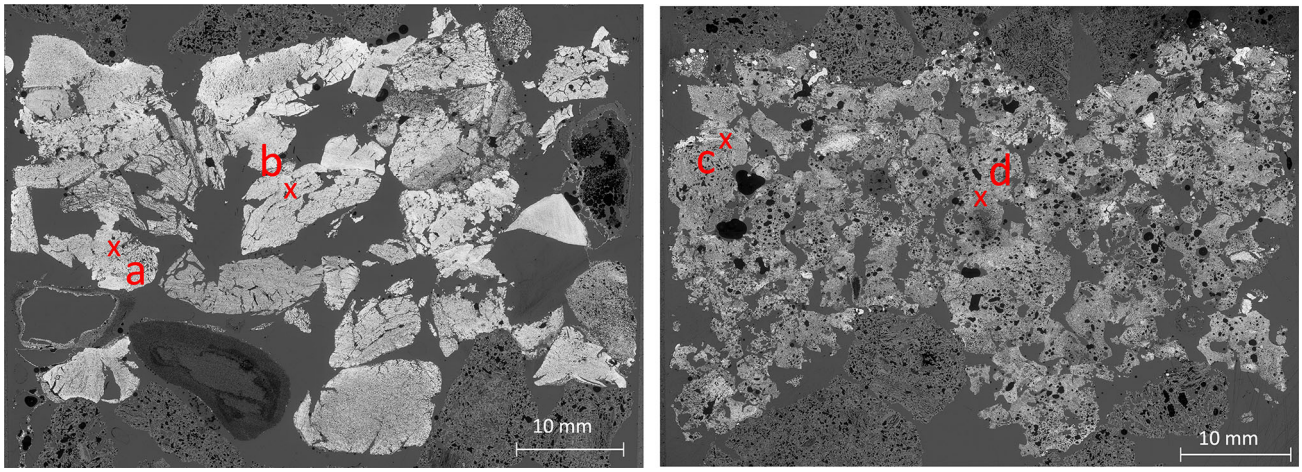

Fig. 17—Reflected light microscopy images of entire softening and melting sample sections under Hydrogen Case gas. Left: NBLL ((*a*) wall particle, (*b*) central particle), Right: SH1 ((*c*) wall particle, (*d*) central particle).

point of the metallic iron does (at least in part) contribute to the observed softening and melting test results reported previously.[22]

By comparison of the NBLL burden under the Base Case and Hydrogen Case gas, it can be observed that for most of the NBLL particles, addition of hydrogen did not promote gas carburization of the metallic iron. However, the presence of a single carburized NBLL particle (away from other sources of carbon) suggests that features conducive to gas carburization may arise in some lump particles. The differentiating features of the carburized lump particle could not be discerned in this study, however, warrant further investigation. Overall, with the lack of carburization in most of the NBLL particles, the melting point of the metallic iron phase remains around 1537 °C. This is consistent with the previously observed physical structure, which showed solid, highly metallic particles for the NBLL burden under the Hydrogen Case gas.[22]

The presence of carbon in the metallic iron effects not only the liquid formation temperature, but also its mechanical strength. As the metallic iron is the primary support and structure for the ferrous burden, its mechanical strength (at temperature) dictates the contraction behavior observed in the softening and melting test. Through hot compression testing (carbon contents ranging from 0.036 to 0.733 wt pct, temperatures between 900 °C and 1200 °C),[34–36] previous studies have suggested that increasing carbon content causes a softening effect at low strain rates[35] (higher rate of dynamic recrystallization[34] and decreased hot deformation activation energy[36]).

From these results, it can be inferred that with the inclusion of hydrogen, highly metallized lump ore retains its structural properties at high temperatures (> 1500 °C), where sinter mechanical strength and melting point may be reduced due to the low temperature (1300 °C) introduction of carbon. As such, in

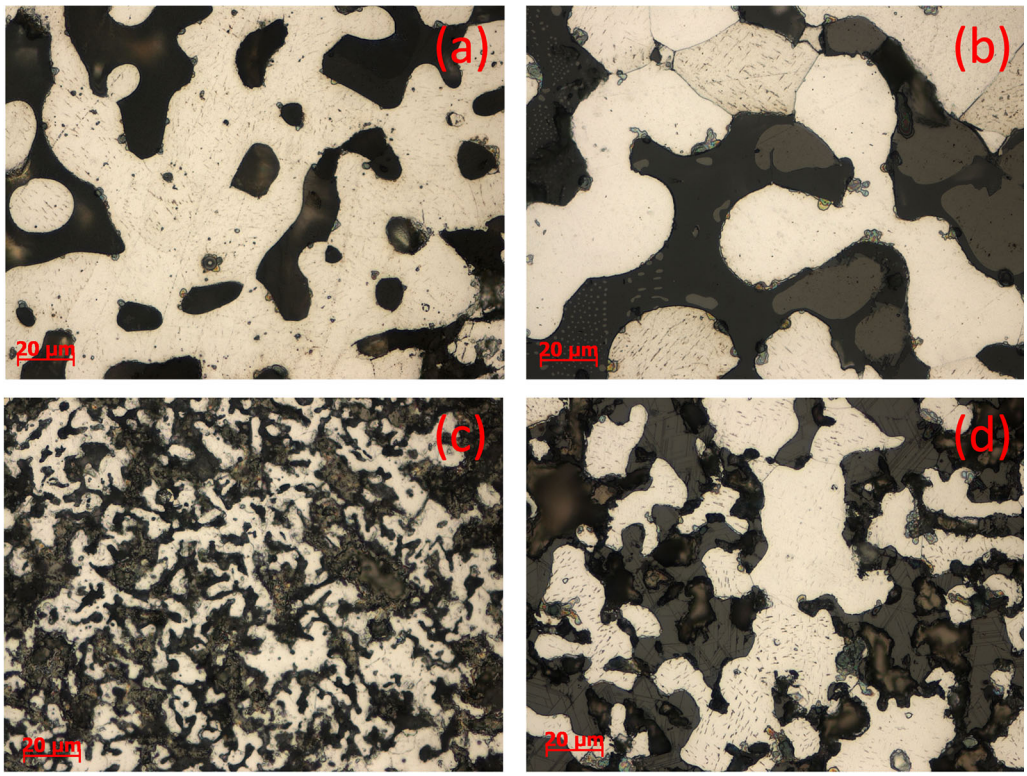

Fig. 18—Metallographic images of NBLL (top row) and SH1 (bottom row) under Base Case gas corresponding to image locations are presented in Fig. 2. ((*a*) NBLL central particle, (*b*) NBLL wall particle, (*c*) SH1 wall particle, (*d*) SH1 central particle).

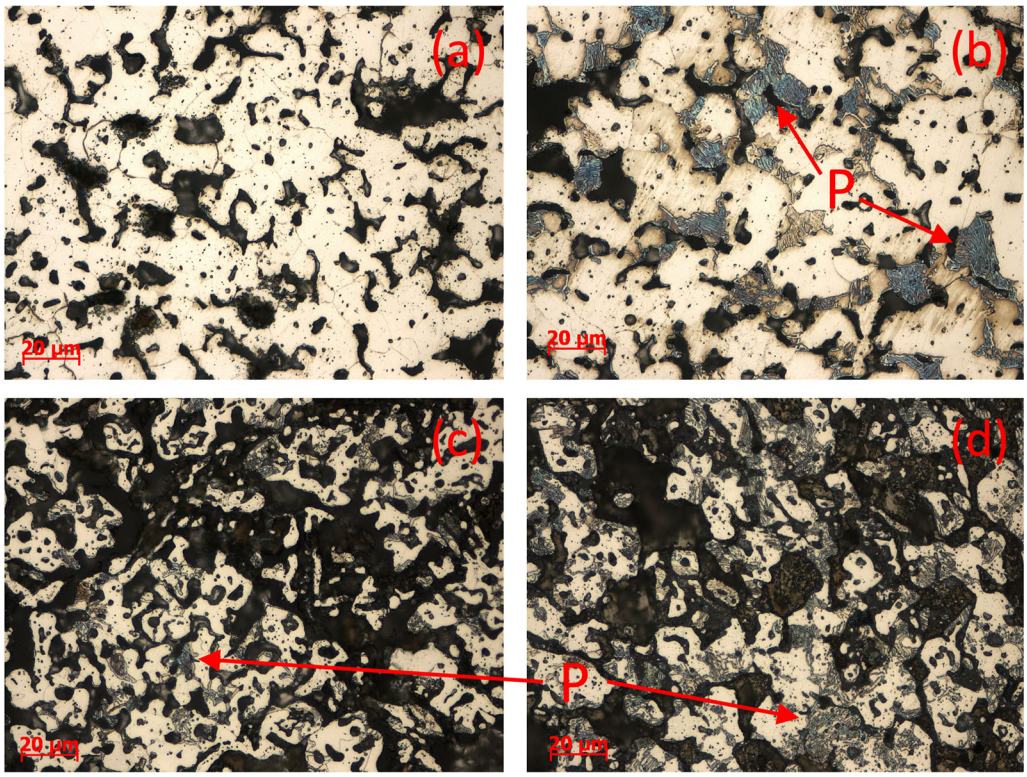

Fig. 19—Metallographic images of NBLL (top row) and SH1 (bottom row) under Hydrogen Case gas corresponding to image locations presented in Fig. 3. ((*a*) NBLL wall particle, (*b*) NBLL central particle, (*c*) SH1 wall particle, (*d*) SH1 central particle). (Example pearlite structures indicated by P).

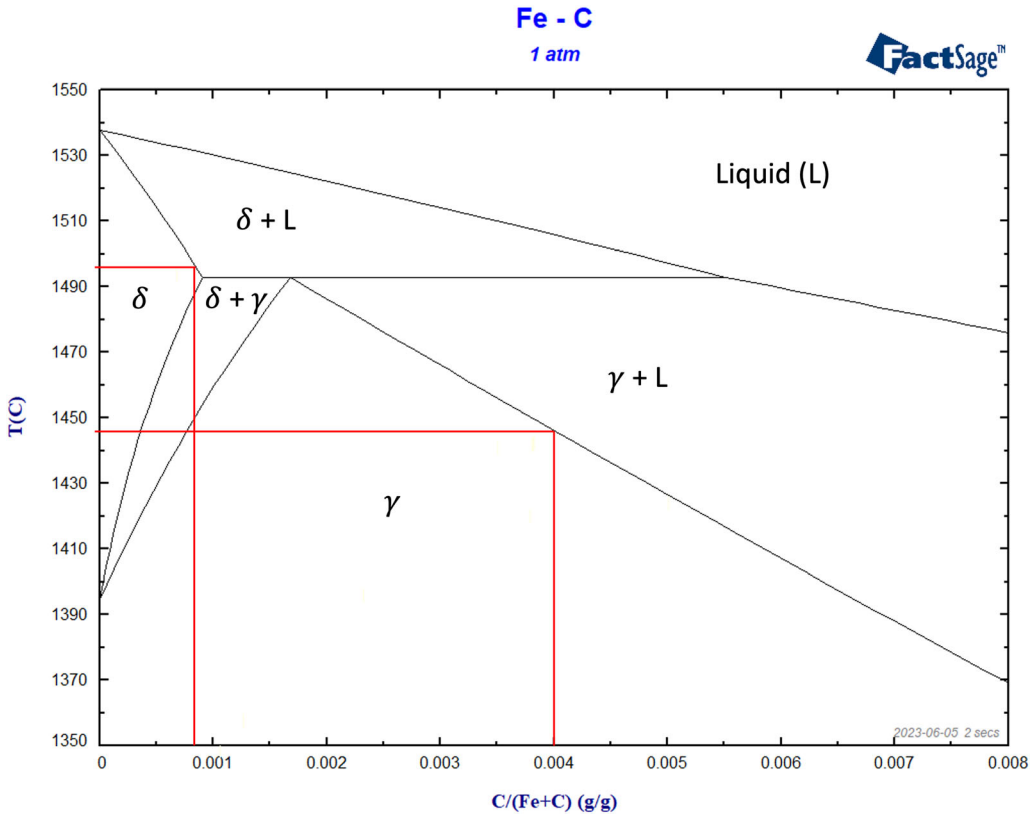

Fig. 20—Portion of the Fe-C phase diagram as calculated by FactSage 8.2 (FSstel database). Red lines indicate observed range of carbon concentrations and associated solidus temperature.

mixed burdens with hydrogen inclusion, lump ore may provide high-temperature physical support to the bed of contracting sinter.

D. *Considerations for Combined Metallic Iron/Slag System*

Through the local assessment of various interfacial conditions, slag interaction mechanisms were analyzed independently to the metallic iron. Additionally, carburization behaviors of the metallic iron were assessed independently to the oxide system. In isolation, these analyses provide a static snapshot of the metallurgical system at the interruption temperature, from which strong conclusions can be drawn about softening and melting performance of mixed burdens. However, with the co-existence of the metal and oxide system within the ferrous burden, they inevitably impact each other. In order to provide context to the results presented thus far and extend the interpretation of the new findings to previously reported softening and melting test results, considerations for the mixed metallic and oxide systems are discussed.

The primary considerations of the mixed oxide and metallic system are related to physical contact conditions between the gas, liquid, and solid phases present. Specifically, the presence of liquid (and its wetting properties on the surrounding material) may impact the contact of gas with the inside of the particle. Wicking of liquid slag into a surrounding metallic network (in the case of metallic rim formation) is known to hinder the rate of reduction,[15,33] however, with the inclusion of hydrogen, gas carburization of iron may also be impacted. As such, while liquid formation in the oxide phase is considered in isolation in this study, the context of these results in a mixed system (in which the liquid properties affect the metallic iron system) should be recognized.

In previously reported softening and melting results, NBLL burden was seen to have a lower maximum pressure drop with the inclusion of hydrogen, where SH1 burden maximum pressure drop increased. Additionally, MB1 was observed to have superior softening and melting performance to both its constituent burdens, indicating that a favorable high-temperature interaction was still occurring between them with the inclusion of hydrogen. Through the detailed analysis of local interfacial conditions in mixed burdens, as well as observation of metal carbon content in individual burdens, a metallurgical description of the observed softening and melting performance changes with hydrogen inclusion can be formed.

Under traditional softening and melting test conditions, metallic iron in both the sinter and lump particles tended to contain no carbon at 1300 °C. At interfaces between lump and sinter at this temperature, primary slag from lump particles (predominantly FeO/SiO_2) had migrated into sinter. Where sufficient magnesium was present within the sinter particle, secondary slag phases solidified such as bredigite, olivine, merwinite, and

melilite. This condition is consistent with mechanisms proposed previously.[7,8,37] Local assessment of real interfaces also revealed new phases under traditional conditions, specifically in magnesium-deficient regions. Where magnesium was not locally present, some larnite and CAF phases were observed in the sinter region, and calcium was observed to migrate into the lump particle, solidifying anorthite.

Addition of hydrogen to the softening and melting test gas impacted both the oxide and metallic phases present in the burden particles at the onset of melting. Comparatively to traditional conditions, lump particles were highly metallized. The high degree of metallization of the lump particles with hydrogen inclusion resulted in significant amounts of metallic iron, which structurally supported the ferrous layer, facilitating gas flow. Additionally, the lower total gangue content of lump (compared with sinter) combined with the decreased amount of FeO resulted in less low-temperature liquids, as well as less total slag. This is conducive to a mechanically strong structure up to high temperatures, consistent with the observed micrographs and softening and melting performance reported previously.[22] At 1300 °C, carbon was only observed in the metallic iron of a single lump particle, however, the metallic iron of sinter was seen to contain significant amounts of carbon. This observation builds on previously reported gas analysis results, which indicated that carbon accumulation was accentuated under the Hydrogen Case gas. The observation of carbon in the metallic iron of the sinter and not lump explains the lower first drip temperatures observed for sinter-based burdens in the softening and melting test, as the melting point of the iron was reduced.[22] In addition to the melting point change, the presence of carbon at 1300 °C may have altered the mechanical strength of the metallic iron, facilitating the contraction (and closing of gas channels) of the sinter burden around this temperature. The liquid formation of the oxide within the sinter was seen to be relatively consistent under both the Base Case and Hydrogen Case gas conditions. As such, the softening of the metal phase may be the primary contributor to the deterioration of the sinter performance under the Hydrogen Case gas.

New mechanisms of slag interaction were observed for highly metallized lump particles in contact with sinter. Where the lump gangue was primarily alumina based, the dominant gangue phase was spinel at 1300 °C, with almost no liquid formation. In this case, only a small interaction region was observed. Where the gangue was silica based, a small amount of liquid (FeO/SiO_2 based) was formed, dictated by the remaining FeO amount. Migration of sinter melts ($FeO/CaO/SiO_2$ based) was observed into the lump region, which reacted with remaining silica in the lump and solidified as rankinite and wollastonite phases. These results indicate that for the highly metallized particles assessed, the interaction is initiated by the sinter primary slag. These results confirm that a favorable high-temperature interaction between lump and sinter still occurs at high metallization degrees, however, the mechanisms are slightly different. The interaction is initiated by liquid formation in the sinter and acts to suppress the primary slags through stabilization of solid secondary slag phases. Liquid formation in the sinter is particularly influenced by the local MgO content, which does not participate strongly in liquid formation at 1300 °C.

The observation of an interaction between lump and sinter explains the significant changes to softening and melting performance observed previously with inclusion of hydrogen.[22] Specifically, the suppression of low-temperature liquid oxide improves the gas permeability, resulting in a lower maximum pressure drop. In combination with the understanding gained from the metal analysis, the addition of lump particles into the sinter burden improves its performance with the inclusion of hydrogen in two ways. Physically, the highly metallic lump particles provide a structural support to the bed of sinter. Chemically, highly metallized lump interfaces provide a region for FeO-rich phases to move and interact, supressing low-temperature liquid formation and resulting in a narrower meltdown temperature range.

IV. CONCLUSION

Samples from lump and sinter mixed burden softening and melting tests interrupted at 1300 °C[22] were analyzed in detail to gain insight into the metallurgical factors influencing observed performance changes with hydrogen inclusion. A novel integrated thermodynamic mapping approach was used to assess the oxide system at the interfaces of sinter with low and high metallization lump particles. Metallographic etching was used to infer changes in gas carburization behavior of the metallic iron within burden particles. The key findings were as follows:

- With the inclusion of hydrogen, the metallic iron in sinter burden showed significant gas carburization around 1300 °C, while the oxide system remained relatively unchanged. This resulted in a metallic iron network with a lower melting point, explaining the observed lowering of the first drip temperature and higher pressure drop.
- With the inclusion of hydrogen, the metallic iron in the majority of the lump burden showed no carbon. The oxide presence was significantly reduced (due to the high metallization achieved), with much lower liquid formation (restricted by remaining FeO). This resulted in structurally strong metallic particles which maintained gas channels, and thus improved softening and melting performance.
- A favorable high-temperature interaction was still observed between lump and sinter slag phases with the inclusion of hydrogen. The mechanism of interaction is largely dependent on local interfacial conditions. Where MgO was locally available in sinter, little liquid formation was observed in either burden (resulting in marginal interaction). Where MgO was not locally available in sinter, the interaction was initiated by sinter primary slags. In this case, the reaction products were calcium silicates (rankinite and wollastonite). Similar to traditional operation,

the interaction acted to suppress lower temperature liquid formation, explaining the improved pressure drop in mixed burdens as compared with the sinter only burden.

- The incorporation of lump in the mixed burdens with hydrogen inclusion provides physical support through the highly metallized lump particles as well as suppression of the sinter primary slags. This improves the performance of the mixed burdens compared to its individual component burdens. As such, burden design in future hydrogen-enriched operations may benefit from increased lump proportions. However, further research is required to determine optimal burden design and to consider whether changes should be made in sinter and pellet quality requirements.

ACKNOWLEDGMENTS

The authors acknowledge industry partner BHP for their financial support and permission to publish this paper.

CONFLICT OF INTEREST

The authors declare that they have no conflict of interest.

FUNDING

Open Access funding enabled and organized by CAUL and its Member Institutions.

OPEN ACCESS

REFERENCES

1. M. Naito, K. Takeda, and Y. Matsui: *ISIJ Int*., 2015, vol. 55, pp. 7–35. https://doi.org/10.2355/isijinternational.55.7.
2. Z. Lu, H. Gu, L. Chen, D. Liu, Y. Yang, and A. McLean: *Ironmak. Steelmak*., 2019, vol. 46, pp. 618–84. https://doi.org/10.1080/03019233.2019.1626112.
3. X. Liu, T. Honeyands, D. O'Dea, J. Chen, and G.-J. Qiu: *Iron Steel Int*., 2019, vol. 54, pp. 19–26. https://doi.org/10.13228/j.boyuan.issn0449-749x.20190094.
4. Y. Wang, J. Diao, B. Xie, C. Qi, and P. Du: *Metals*, 2022, vol. 12, p. 987. https://doi.org/10.3390/met12060987.
5. S. Wu, Y. Lu, Z. Hong, and H. Zhou: *ISIJ Int*., 2020, vol. 60, pp. 1504–11. https://doi.org/10.2355/isijinternational.ISIJINT-2019-833.
6. S. Wu, H. Han, H. Xu, H. Wang, and X. Liu: *ISIJ Int*., 2010, pp. 686–94. https://doi.org/10.2355/isijinternational.50.686.
7. X. Liu, S. Wu, W. Huang, K. Zhang, and K. Du: *ISIJ Int*., 2014, vol. 54, pp. 2089–96. https://doi.org/10.2355/isijinternational.54.2089.
8. X. Liu, T. Honeyands, G. Evans, D. O'Dea, and B. Ellis: in *8th International Congress on Science and Technology of Ironmaking*, Vienna, 2018, pp. 583–9.
9. X. Liu, T. Honeyands, G. Evans, J. Chen, and D. O'Dea: in *Iron Ore Conference*, Perth, 2019, pp. 872–9.
10. Y. Lu, S. Wu, B. Du, and H. Zhou: *ISIJ Int*., 2020, vol. 60, pp. 1461–8. https://doi.org/10.2355/isijinternational.ISIJINT-2019-713.
11. L. Chen, Q. Xue, W. Guo, X. She, and J. Wang: *Ironmak. Steelmak*., 2016, vol. 43, pp. 458–93. https://doi.org/10.1080/03019233.2015.1104074.
12. P.C. Hayes: *Steel Res. Int*., 2011, vol. 82, pp. 480–93. https://doi.org/10.1002/srin.201100032.
13. S.-H. Kim, X. Zhang, Y. Ma, I.R. Souza Filho, K. Schweinar, K. Angenendt, D. Vogel, L.T. Stephenson, A.A. El-Zoka, J.R. Mianroodi, M. Rohwerder, B. Gault, and D. Raabe: *Acta Mater*., 2021, vol. 212, p. 116933. https://doi.org/10.1016/j.actamat.2021.116933.
14. W. Guo, Q. Xue, Y.L. Liu, X. She, and J. Wang: *Ironmak. Steelmak*., 2016, vol. 43, pp. 22–30. https://doi.org/10.1179/1743281215Y.0000000043.
15. I. Vemdrame Flores, O. Matos, A. Lima da Silva, and M. CovcevichBagatini: *Metall. Mater. Trans. B*, 2021, vol. 52B, pp. 1716–38. https://doi.org/10.1007/s11663-021-02140-7.
16. S.J. Chew, P. Zulli, R. Nightingale, and A. Yu: in *SCANMET II*, Lulea, Sweden, 2004, pp. 405–16.
17. K. Jiao, G. Feng, J. Zhang, C. Wang, and L. Zhang: *Energy*, 2023, vol. 263, p. 125518. https://doi.org/10.1016/j.energy.2022.125518.
18. A.A. Ei-Geassy, K.A. Shehata, and S.Y. Ezz: *Trans. Iron Steel Inst. Jpn*., 1977, vol. 17, pp. 629–35. https://doi.org/10.2355/isijinternational1966.17.629.
19. Z. Wang and R.A. Yetter: *Int. J. Chem. Kinet*., 2009, vol. 41, pp. 327–36. https://doi.org/10.1002/kin.20407.
20. H. Ono, K. Tanizawa, and T. Usui: *ISIJ Int*., 2011, vol. 51, pp. 1274–8. https://doi.org/10.2355/isijinternational.51.1274.
21. Y. Qie, Q. Lyu, X. Liu, J. Li, C. Lan, S. Zhang, and C. Yan: *Metall. Mater. Trans. B*, 2018, vol. 49B, pp. 2622–32. https://doi.org/10.1007/s11663-018-1299-3.
22. N. Barrett, S. Mitra, S. Chew, D. O'Dea, and T. Honeyands: *ISIJ Int*., 2023, pp. 1626–36. https://doi.org/10.2355/isijinternational.ISIJINT-2023-190.
23. K. Raipala: Helsinki University of Technology (2003).
24. K. Geels, D. Fowler, W. Kopp, and M. Ruckert: *Metallographic and Materialographic Specimem Preparation, Light Microscopy, Image Analysis and Hardness Testing*, ASTM International, Pennsylvania, 2007.
25. S. Wu, B. Su, X. Liu, and M.Y. Kou: *Ironmak. Steelmak*., 2018, vol. 45, pp. 50–7. https://doi.org/10.1080/03019233.2016.1237073.
26. C. Lan, S. Zhang, X. Liu, Q. Lyu, and M. Jiang: *Int. J. Hydrogen Energy*, 2020, pp. 14255–65. https://doi.org/10.1016/j.ijhydene.2020.03.143.
27. M.M. Hoque, H. Doostmohammadi, S. Mitra, D. O'Dea, X. Liu, and T. Honeyands: *ISIJ Int*., 2021, vol. 61, pp. 2944–52. https://doi.org/10.2355/isijinternational.ISIJINT-2021-198.
28. L. Ma, J. Zhang, Y. Wang, M. Lu, Q. Cai, C. Xu, Z. Li, and Z. Liu: *Powder Technol*., 2022, vol. 412, p. 117979. https://doi.org/10.1016/j.powtec.2022.117979.
29. B.-B. Lyu, G. Wang, F. Yang, H.-B. Zuo, Q.-G. Xue, and J.-S. Wang: *J. Iron. Steel Res. Int*., 2023, pp. 2366–77. https://doi.org/10.1007/s42243-023-00951-3.

30. B. Lyu, F. Yang, G. Wang, H. Zuo, Q. Xue, and J. Wang: *Advances in Pyrometallurgy*, Springer, Cham, 2023, p. 95–106.
31. TESCAN: TESCAN TIMA for Mineral Processing. https://www.tescan.com/product/tescan-sem-solutions-tescan-tima-for-mineral-processing/ (14/08/2023).
32. J.M.F. Clout, and J.R. Manuel: in *Iron Ore*, 2nd ed., L. Lu, ed., Woodhead Publishing, Cambridge, 2022, pp. 59–108.
33. T. Bakker, and R. Heerema: in *International Congress on the Science and Technology of Ironmaking (ICSTI)*, Toronto, 1998, vol. 57, pp. 1597–608.
34. S. Serajzadeh and A. Karimi Taheri: *Mater. Des.*, 2002, vol. 23, pp. 271–6. https://doi.org/10.1016/S0261-3069(01)00080-2.
35. H. Zhao, J. Qi, G. Liu, R. Su, and Z. Sun: *J. Market. Res.*, 2020, vol. 9, pp. 11319–31. https://doi.org/10.1016/j.jmrt.2020.08.016.
36. P. Kawulok, P. Opěla, I. Schindler, R. Kawulok, S. Rusz, M. Sauer, and K. Konečná: *Materials*, 2022, vol. 15, p. 595. https://doi.org/10.3390/ma15020595.
37. X. Liu, T. Honeyands, G. Evans, P. Zulli, and D. O'Dea: *Ironmak. Steelmak.*, 2019, vol. 46, pp. 953–67. https://doi.org/10.1080/03019233.2018.1464107.